A mechanical knock-out system uncovers that loss of titin tension triggers muscle disease

Roberto Silva-Rojas[a,*], Natalia Vicente[a], Manuel Gavilán-Herrera[a], Verónica Labrador-Cantarero[a], Jon Sicilia[a], Olga Giménez-Sáez[a], Andra C. Dumitru[a,b], Mateo I. Sánchez[c], Mara Gato-Vilaseca[a], Diana Velázquez-Carreras[a], Juan Antonio López[a,d], Jesús Vázquez[a,d], Elías Herrero-Galán[a], Miguel A. López-Unzu[a], Maria Rosaria Pricolo[a], Jorge Alegre-Cebollada[a,*]

[a] Centro Nacional de Investigaciones Cardiovasculares (CNIC), Calle de Melchor Fernández Almagro 3, Madrid, Spain

[b] Louvain Institute of Biomolecular Science and Technology, Universite catholique de Louvain, Louvain-la-Neuve, Belgium

[c] University of Cambridge, Department of Chemistry, Lensfield Road, Lensfield Road CB2 1EW, Cambridge (UK)

[d] CIBER de Enfermedades Cardiovasculares (CIBERCV), Madrid, Spain

[*]Correspondence: Roberto Silva-Rojas (rsilvar@cnic.es) and Jorge Alegre-Cebollada (jalegre@cnic.es; @AlegreCebollada)

Abstract

Mechanical proteins such as titin, the elastic shaft of muscle sarcomeres, are typically multifunctional and at the basis of the development of disease including complex mechanosignaling mechanisms that are incompletely understood. Here, we introduce site-directed polypeptide severing to cease force transmission across titin *in vivo*, an approach that we term mechanical knock-out (mKO) since it focuses on the evaluation of the mechanical function of the targeted protein. When induced in homozygosis, titin mKO muscles develop marked atrophy, depressed force generation and substantial transcriptional dysregulation. mKO myofibers, although persistent, shrink and undergo progressive sarcomere depletion correlating with altered levels of muscle-atrophy-related titin interactors including rapid MuRF1 upregulation. Affected fibers also display mitochondria aggregation and internalization of myonuclei, which is preceded by desmin mislocalization. Milder phenotypes in heterozygous mKO muscles closely resemble human myopathy caused by titin mutations. Our results uncover that slack titin molecules trigger disease, prospectively by mechanisms shared with other mechanical proteins.

Keywords: muscle, mechanobiology, mechanical knock-out, myopathy, titin

Main

In cells, many multifunctional proteins must work under mechanical tension, including talin and α-catenin at the basis of mechanosensing and mechanotransduction in adhesion sites[1,2]; lamin, a guardian of nuclear integrity[3]; and dystrophin, which ensures efficient force transmission in striated muscle and is mutated in Duchenne muscular dystrophy[4]. Despite remarkable progress using *in vitro* systems, current knowledge on the integrative mechanical functions of proteins *in vivo* remains incomplete. An important limitation in this regard is that loss of protein levels in conventional knock-out (KO) or knock-down approaches results in the suppression of both the mechanical and non-mechanical functions of the targeted protein, complicating interpretation of results (**Figure 1A**)[5-11].

In this work, we focus on titin, another paradigmatic example of a protein with coexistent mechanical and non-mechanical functions[12]. With a giant size of up to 3.8 MDa and connecting the Z- and M-lines of sarcomeres (**Figure 1B**), titin is the major contributor to the passive stiffness of muscle tissue at physiological levels of stretch[13,14]. In addition to these structural and mechanical roles, titin domains also serve as binding hubs for protein partners that regulate muscle hypertrophy/atrophy[10,11,14,15]. Of note, the longitudinal location of titin in sarcomeres makes it a prime candidate to integrate muscle cell responses to mechanical forces, which have been shown *in vitro* to change the affinity of titin for its interactors[16,17], modulate mechanosignaling pathways at the M-line region of the protein[18-21], and enable posttranslational modifications that modulate titin mechanics[22].

Consistent with the fundamental functions of the protein, truncating variants in the titin gene (*TTN*) are responsible for many severe diseases including dilated cardiomyopathy[23] and congenital myopathies[24-26]. However, the underlying molecular pathomechanisms remain largely unknown[27]. Recently, truncated titin molecules have been observed to be incorporated into cardiac sarcomeres, although in a less stable manner than wild-type (WT) counterparts potentially compromising force transmission[28,29]. Considering also that sarcomere stability *ex vivo* requires that the mechanical integrity of titin is preserved[30,31], it is plausible that loss of mechanical transduction across the protein could contribute *per se* to the pathogenic load of truncating *TTN* variants, a tantalizing hypothesis that remains untested.

To dissect the functional role of titin mechanics, here we exploit site-directed cleavage of the protein by heterologous expression of Tobacco Etch Virus protease (TEVp) in living mice (**Figure 1A,B**). This strategy, which we name titin mechanical KO (mKO), results in loss of force transduction across titin's polypeptide backbone while preserving the total levels of the protein and therefore its non-mechanical functions. For implementation, we used TEVs-TTN mice carrying the TEVp recognition site in the I-band of titin[32], a model employed before for *ex vivo* studies confirming the major contribution of titin to muscle cell stiffness[31,33,34] and uncovering the role of titin-based force on myofilament structure, regulation and stability[31,35-37], as well as for examination of sarcomere turnover in cultured cardiomyocytes and *in vivo* via HaloTag chemistry[38]. Here, we demonstrate that TEVp-directed severing can be applied to study the mechanical contribution of proteins to organ physiology *in vivo*. Our results reveal that titin mKO muscles develop a severe form of myopathy

recapitulating a number of structural, histological and functional phenotypes in human patients who carry pathogenic *TTN* variants. Unexpectedly, we also find that titin mechanical integrity is required for stable positioning of myonuclei, and demonstrate the viability and long-term persistence of sarcomere-free, titin mKO myofibers.

Results

Titin mechanical knock-out induces loss of muscle mass and strength

To implement titin mKO, we injected AAV6 viral vectors encoding a GFP-tagged version of a TEV protease with optimized catalytic activity (GFP-TEVp)[39] into the tibialis anterior (TA) and extensor digitorum longus (EDL) muscles of homozygous TEVs-TTN mice[32]. Vehicle saline buffer was injected in contralateral legs, which served as internal controls (**Figure 1B**). To ensure specificity of phenotypes resulting from titin mKO, we also treated WT mice (**Figure 1B**). Using western blot (WB) and immunofluorescence, we verified time-dependent accumulation of GFP-TEVp in AAV6-injected legs from both WT and TEVs-TTN mice (**Figures 1C, S1A-C**). We noted that GFP-TEVp levels are higher in TEVs-TTN muscles, probably reflecting substrate-mediated stabilization of the protease since mRNA levels of the transgene do not follow the same trend (**Table S1**).

Next, we assessed titin levels and cleavage using low percentage SDS-PAGE gels and titin peptide fingerprinting by mass spectrometry (**Figures 1D-G**). Results reveal progressive loss of full-length ~3.8 MDa N2A titin only in AAV6-injected, TTVs-TTN muscles (**Figure 1F**). Concomitantly, we observed the appearance of a ~2.2 MDa A-M titin fragment with slightly higher mobility than naturally present T2/Cronos titin, and ~1.6 MDa Z-I fragments as expected from the existence of alternatively spliced forms of titin in the I-band of the protein (**Figure 1D,G**)[32]. Importantly, AAV6-injected TEVs-TTN muscles show preserved titin protein levels (**Figure 1E**). As expected from the loss of titin mechanical integrity, AAV6-injected TEVs-TTN myofibers display 35-65% drop in passive stiffness at 7 days post-infection (dpi), an effect that is not observed in WT samples (**Figure 1H,I**)[31].

At the tissue level, titin mKO muscles show noticeable atrophy from 7 dpi, an effect that reaches 38% mass loss at 21 dpi (**Figure 1J**). In addition, AAV6-injected TEVs-TTN muscles generate less active force than WT counterparts at 7 dpi even when data are normalized by muscle cross sectional area, a result that cannot be explained by a tendency to slightly lower force generation of TEVs-TTN muscles in basal conditions (**Figure 1K,L, S1D-E**). In contrast, titin mKO does not result in detectable alterations of contraction kinetics (**Figure S1F**).

Altogether, our results indicate that titin mKO leads to atrophy and reduced force generation of targeted muscles. These effects are not observed in controls where GFP-TEVp is expressed in WT animals.

Histopathological features of titin mechanical knock-out muscles

The phenotypes we observe in titin mKO muscles appear to happen in the absence of remarkable myofiber death. Indeed, we only have limited evidence of titin-mKO-induced necrosis at 3 dpi, when 6.5% of myofibers show IgG infiltration (**Figure S2A**)[40]. To further characterize the myopathic response in titin mKO muscles, we did histological staining routinely used to classify congenital myopathies. We first stained sections with hematoxylin-eosin (HE) (**Figure 2A**) or wheat germ agglutinin (WGA) (**Figure S1A**). Results demonstrate a

shift towards smaller myofiber size at 7 and 21 dpi only in titin mKO muscles (**Figure 2B**), which is evidenced by 40-60% less myofibers with minimal Feret diameter (MinFeret) larger than 30 µm (**Figure 2C**). Strikingly, our results reveal a marked increase of myofibers with internalized myonuclei in titin mKO muscles, which is already evident at 3 dpi (**Figure 2A,D**). In some AAV6-injected WT muscles at 21 dpi, we also detect internal myonuclei. We hypothesize that these internal myonuclei probably belong to new, immature myofibers resulting from muscle regeneration induced by non-specific GFP-TEVp immunogenicity as observed in other settings[41]. Consistent with this interpretation, we find that most central myonuclei in AAV6-injected WT are found in GFP-TEVp-negative myofibers, a population expected to be enriched in regenerative myofibers where non-replicative AAV6 particles have been diluted during progenitor cell divisions (**Figure S2B**). In contrast, central myonuclei are found both in GFP-negative and GFP-positive cells in titin mKO muscles (**Figure S2B**). These results support that many myofibers with internal myonuclei in the AAV6-injected TEVs-TTN group do not come from regeneration and that myonuclei internalization in these myofibers is a direct consequence of titin cleavage. Accordingly, mislocalization of desmin intermediate filaments is present in ~40% of AAV6-injected TEVs-TTN myofibers already at 3 dpi (**Figure 2E-F**, **S2C**), and therefore precedes nuclear centralization in many cases (**Figure 2D**) as observed in centronuclear myopathy, a muscle disorder where the presence of central myonuclei is unrelated to myofiber regeneration[42]. Importantly, no overt desmin mislocalization is detected in AAV6-injected WT muscles (**Figure 2F, S2C**), providing additional support that myonuclei internalization induced by GFP-TEVp expression in WT animals is related to immunogenicity-related muscle regeneration.

We extended histological characterization using succinate dehydrogenase (SDH) staining, which shows mitochondrial aggregates in titin mKO samples from 3 dpi. These aggregates become centralized from 7 dpi eventually resulting in a halo-ring appearance of many myofibers at 21 dpi (**Figure 2G**). Complementary nicotinamide adenine dinucleotide dehydrogenase (NADH) staining confirms mitochondrial alterations in titin mKO specimens (**Figure S3A**). In addition, Gomori staining detects dye-free, irregular regions induced by titin mKO (**Figure S3B**). Although this result could be compatible with the presence of intracellular vacuoles, we do not observe typical signs of vacuolization in HE staining (**Figure 2A**). Gomori also reveals increased interfiber spacing in titin mKO samples (**Figure S3B**). In agreement with this observation, we find that titin mKO sections show increased picrosirius staining from 7 dpi, indicative of interstitial fibrosis (**Figure S3C**).

In combination, our histological characterization demonstrates that titin mKO muscles develop common histopathological features of muscle disease, including myofiber atrophy, myonuclei internalization, mitochondrial mislocalization and fibrosis[24-26].

Heterozygous titin mechanical knock-out muscles display milder phenotypes

To study consequences of titin mKO in heterozygosis, we injected independent cohorts of homozygous and heterozygous TEVs-TTN mice with GFP-TEVp-expressing AAV6 vectors. Both groups show equivalent expression of GFP-TEVp in injected muscles at 7 dpi (**Figure 3A, S4A,B**), which results in preserved titin levels but 68% and 24% titin cleavage in homozygous and heterozygous samples, respectively (**Figure 3B-D**).

Consistent with our results in **Figure 1J**, homozygous titin mKO muscles weigh 16% less than control counterparts at 7 dpi (**Figure S4C**). In contrast, AAV6-injected heterozygous TEVs-TTN muscles do not show any evidence of weight loss (**Figure S4C**) although the fraction of myofibers with MinFeret larger than 30 µm is reduced by 25% (**Figures 3E, S4D**). Remarkably, myofibers in heterozygous titin mKO muscles have higher fraction of central myonuclei than controls; an effect that correlates with the extent of desmin mislocalization (**Figure 3F-I**). Both effects are not as pronounced as in titin mKO homozygous animals. At the histological level, histological staining with SDH (**Figure 3J**) and NADH (**Figure S4E**) reveals cores in heterozygous titin mKO samples. We also observe dye-free regions in Gomori (**Figure S4F**). Overall, our results indicate that induction of titin mKO in heterozygosis results in a milder form of myopathy as compared to homozygous conditions.

Titin mechanical knock-out leads to sarcomere disassembly

Having verified the effects of titin mKO at the tissue and cellular levels, we next examined the underlying sarcomere alterations. Mechanically, titin can be divided into two main regions (**Figure 4A**). While A-band titin is an integral part of the thick filament participating in fundamental structural interactions[43,44], the I-band of the protein has a prominent mechanical role thanks to the ability of I-band domains to adapt their extension to the fluctuating force experienced or generated by sarcomeres[45]. TEVs-TTN muscle contains the TEV protease cleavage site at the end of the I-band part of titin (**Figure 4A**); hence, we hypothesized that releasing force upon titin cleavage by TEV protease would primarily affect titin's I-band. We did fluorescent immunohistochemistry on longitudinal muscle sections using antibodies against alpha-actinin (labeling the Z-disk of sarcomeres), the PEVK region within I-band titin, and the cleaved TEV site (cTEVsite) (**Figure 4A**; validation of specificity of anti-cTEVsite shown in **Figure S5A,B**). At 3 dpi, muscles from the three control groups display normal PEVK immunostaining resulting in two maxima flanking the Z-disk (**Figure 4B,C**). In contrast, the PEVK epitope shows a single, broader maximum colocalizing with the Z-disk in titin mKO myofibers that are positive for cTEVsite (**Figure 4B,C**). In these myofibers, the cTEVsite signal also locates to the Z-disk **(Figure 4B,C**). These results indicate that the cleaved I-band of titin retracts towards the Z-disk of targeted sarcomeres upon tension release, as observed also *in vitro*[31]. Interestingly, this recoiling occurs in a context where overall sarcomeric structure is well preserved according to Z-disk staining (**Figure 4B**). At 7 and 21 dpi, sarcomere organization is completely lost in most myofibers of the homozygous titin mKO group (**Figure 4B**).

To characterize sarcomere disassembly induced by titin mKO at higher resolution, we assessed muscle ultrastructure by transmission electron microscopy (TEM). TEM micrographs show that homozygous titin mKO muscles display focal disarray of sarcomeric structure already at 3 dpi (**Figure 4D**). In agreement with the immunofluorescence results in **Figure 4B**, no evidence of organized sarcomere structure is observed at 7 and 21 dpi in most myofibers of the homozygous titin mKO group (**Figure 4D**). We also find limited sarcomere disassembly in heterozygous titin mKO samples at 7 dpi (**Figure S5C**). Electron microscopy images also reveal mitochondrial aggregation in affected homozygous titin mKO myofibers (**Figure S5D**), consistent with

179 histological determinations (**Figure 2G, S3A**). Membrane whorls or multilamellar bodies (MLB) are also found
180 in micrographs of homozygous titin mKO samples (**Figure S5D**).

181 Altogether, immunofluorescence and ultrastructural characterization confirm that titin cleavage by TEV
182 protease results in mechanical unloading of the protein preceding sarcomere disassembly. As a result, many
183 myofibers in titin mKO muscles are fully devoid of sarcomeres from 7 dpi.

184 ## Coexistence of regenerative and titin mechanical knock-out myofibers

185 Our data so far suggest that sarcomere-free, titin mKO myofibers remain viable at 21 dpi, although they shrink
186 and display central myonuclei. We examined the long-term persistence of these myofibers in the context of
187 muscle regeneration (**Figure 5A**). With this aim, we analyzed by immunohistochemistry 21,720 individual
188 TEVs-TTN myofibers and quantified their size, myonuclei position and cTEVsite signal including also samples
189 obtained at 92 dpi (**Figure 5B**). Myofibers in non-injected controls are cTEVsite-negative and show peripheral
190 myonuclei (**Figure 5B,C**). In contrast, a population of infected myofibers displaying high cTEVsite signal
191 marking titin cleavage is evident from 3 dpi onwards (**Figure 5B,C**). These cTEVsite-positive myofibers show
192 progressively reduced size and more centralized myonuclei as time passes (**Figure 5C,D,E**). Remarkably, a
193 population of cTEVsite-negative myofibers with central myonuclei and preserved size becomes apparent at 92
194 dpi. We hypothesize this new population corresponds to myofibers originating from muscle regeneration
195 (**Figure 5C,F,G**). Indeed, using a Pax7 lineage tracing strategy based on the inducible expression of a Tomato
196 reporter that therefore labels myofibers originating from myofiber regeneration[46,47] (**Figure 5H**), we verified
197 the existence of 4.4% regenerative myofibers in the AAV6-injected-TEVs-TTN group already at 21 dpi (**Figure**
198 **5I**). Remarkably, this level of muscle regeneration agrees well with the proportion of cTEVsite-negative
199 myofibers showing central myonuclei at 21 dpi in **Figure 5C**.

200 Taken together, our results confirm that titin mKO is a direct trigger of myofiber atrophy and myonuclei
201 internalization, and that affected cells are only slowly taken over by intact-titin-containing myofibers (**Figure**
202 **S6A**) that originate from muscle regeneration This replenishment of myofibers correlates with a slight recovery
203 of muscle mass at 92 dpi (**Figure S6B**).

204 ## Altered titin interactors in titin mechanical knock-out muscles

205 Considering that titin is a signaling hub that interacts with many proteins relevant for muscle function[14] (**Figure**
206 **6A**), and that the levels of some of these interactors are altered in muscles with stiffer titins[7-9], we hypothesized
207 that titin unloading could perturb titin interactors contributing to downstream myopathic responses. Using WB,
208 we assessed the levels of five titin interactors that are involved in muscle atrophy/hypertrophy and response to
209 stress (**Figure 6B**). At 21 dpi in homozygous titin mKO muscles, we detect increased levels of ANKRD1
210 (**Figure 6C**), a transcriptional coregulator that has been observed to link titin to the thin filament, and is also
211 upregulated in several stress conditions such as intensive care unit-acquired weakness, denervation and
212 dystrophy[48-50]. Interestingly, from 7 dpi in titin mKO muscles we detect increased levels of autoprocessed and
213 active calpain-3, a titin-interacting protease involved in protein turnover and known to cleave ANKRD1[51]

(**Figure 6D**). Total levels of calpain-3 remain unaltered (**Figure S7A**). In agreement with higher calpain-3 activity, the presence of cleaved ANKRD1 is also evident from 7 dpi (**Figure 6E**). The levels of chaperones HPS27 and αβ-crystallin and the ubiquitin ligase MuRF1, all of them involved in protein homeostasis[14,16,52,53], are increased in titin mKO muscles at 21 dpi (**Figure 6F-H**). Remarkably, increased expression of MuRF1 in titin mKO samples is detected as soon as 3 dpi (**Figure 6H**). At this time point, the protein remains at the M-line of sarcomeres (**Figure S7B**). From 7 dpi MuRF1 staining in titin mKO cells becomes disorganized as expected from the absence of noticeable sarcomere structure (**Figure S7B**). We also measured levels of FHL1, a transcriptional co-activator regulating skeletal muscle mass[54], and found the protein to be upregulated by 21 dpi in titin mKO muscles (**Figure S7C**). Intriguingly, basal levels of HSP27, αβ-crystallin and FHL1 levels are increased in TEVs-TTN mice compared to WT counterparts, indicating that the 35 KDa insert in TEVs-TTN may lead to some baseline stress. The mechanisms underlying this phenotype in TEVs-TTn muscles remain unknown, although we speculate they may result from softening of the titin filament from the extra length of the TEVs-containing insert and/or alteration of protein-protein interactions involving the insertion site.

Considering the early alteration of MuRF1 in titin mKO muscles, we assessed whether MuRF1 inhibition could block the myopathic response induced by titin cleavage (**Figure S8**). However, we found that oral treatment with MuRF1 inhibitor MyoMed205, a compound that limits atrophy in heart failure with preserved ejection fraction (HFpEF)[55], muscle disuse[56] and tumor cachexia associated myopathy[57], was not able to normalize levels of MuRF1 (**Figure S8B)**, global protein ubiquitination (**Figure S8C-D**), and myofiber size (**Figure S8E**) in titin mKO samples.

Pathological transcriptional signatures of titin mechanical knock-out muscles

To examine transcriptional changes induced by titin mKO, we did RNAseq analysis of the four experimental groups at 3, 7 and 21 dpi, including also heterozygous samples at 7 dpi. Principal component analysis (PCA) reveals a progressive change in the transcriptional state of homozygous titin mKO muscles starting at 3 dpi, which reaches 5,821 differentially expressed genes (DEGs) at 21 dpi (**Figure 7A, Figure S9A**). In addition, PCA also detects transcriptional alterations in heterozygous titin mKO muscles (**Figure 7A**). Consistent with our histology results, expression of TEV protease in WT animals leads to measurable changes in gene expression by PCA, but only at 21 dpi (**Figure S9B**). To capture specific transcriptional responses induced by titin mKO, for all downstream analyses we removed DEGs shared with the WT group, which mostly belong to Gene Ontology (GO) terms related to immune function as expected (**Figure S9A**). Gene set enrichment analysis[58] shows upregulation of terms related to protein biogenesis in titin mKO muscles at all time points, both in homozygosis and heterozygosis conditions (**Figure 7B, S9C**). In agreement with histology results, we also find that titin mKO leads to upregulation of terms related to fibrotic processes and a consistent downregulation of terms related to mitochondria (**Figure 7B, S9C**). Remarkably, GO analyses detect common overexpression of genes involved in fibrosis and cytoskeletal remodeling and downregulation of genes related to mitochondrial activity in both titin mKO muscles and in samples from the classical titinopathy *mdm* mouse model (**Figures**

7C-E, S9D-F)[59]. Indeed, 47-68% of DEGs in titin mKO muscles show also altered expression in the *mdm* mice, indicative of similar transcriptional states in these two models (**Figures 7C, S9D-F**).

Discussion

Titin, the largest protein known so far, plays multiple fundamental roles in cardiac and skeletal muscle. These range from providing structural support and passive stiffness to sarcomeres, to facilitating assembly of signaling hubs that control muscle physiology[10,11,14,15]. In addition, titin can be considered as a homeostatic integrator of mechanical signals, as indicated for example by the striking capacity of muscle to balance sarcomere length and longitudinal hypertrophy to keep force across titin constant[5]. However, understanding how these mechanical mechanisms involving titin operate *in vivo* has proven challenging, a situation that is shared with other proteins with mechanical function.

Here, we demonstrate that cessation of force transmission across titin results in severe muscle atrophy and dysfunction correlating with gradual sarcomere depletion (**Figure 1, 4**). A corollary of this result is that myofibers do not have redundant mechanisms that can effectively compensate for the loss of titin's mechanical function, implying that every single peptide bond out of the several thousands in titin can be regarded as an Achilles heel of muscle tissue. Remarkably, phenotypes stemming from titin mKO rapidly propagate to compartments other than the sarcomere, including the mitochondria, the nucleus and the extracellular matrix (**Figure 2, S3**). An unexpected finding in this regard is that the mechanical integrity of titin is required to stabilize peripheral location of myonuclei, a function that complements the described role of active sarcomeres driving myonuclei positioning during myofiber formation[60]. Another striking result is the notable persistence of titin mKO myofibers, which are only partially taken over by regenerating counterparts in a timescale of months (**Figure 5**). Considering that targeted EDL and TA muscles contribute little to the physiological state of animals, the local delivery of TEV protease that we have followed ensures that the phenotypes we capture do not result from global perturbation of organismal homeostasis, in agreement with the lack of noticeable effects in control contralateral legs in AAV6-injected TEVs-TTN mice compared to WT counterparts.

In recent years, gene variants in *TTN* have been linked to a growing number of human muscle dystrophies, including tibial muscle dystrophy (TMD)[61-63], limb girdle muscle dystrophy (LGMD R10 titin-related)[64], Emery-Dreifuss-like dystrophy[65], hereditary myopathy with early respiratory failure (HMERF)[66,67], and congenital myopathies such as centronuclear myopathy[68] and autosomal recessive multi-minicore disease with heart disease (AR MmD-HD)[69] . Indeed, the term titinopathies is now used to refer to all the above forms of muscle disease when they are caused by titin mutations[24]. Together with the different types of heart disease triggered by titin variants[70], the existence of titinopathies make *TTN* an important human disease gene. In this context, the histological similarities of titin mKO muscles with human counterparts affected by titinopathy are remarkable. For instance, sarcomere disorganization, myofiber size variability, central myonuclei, altered mitochondrial organization and fibrosis are typical features of most titinopathies[24-26]; we find all of them in titin mKO muscles (**Figures 2,4**). This resemblance is particularly striking in the case of heterozygous titin mKO

samples, which also show cores in SDH staining and electron microscopy **(Figures 3, S4E, S5C**)[24,68]. Furthermore, gene expression profiles induced by titin mKO and in titinopathy muscles overlap to a considerable extent (**Figures 7C-E, S9D-F**). Considering these similarities and the fact that truncated titins recoil toward the Z-disk under force[29], a phenotype also observed in mKO titins **(Figure 4B,C**), we speculate that loss of mechanical transduction across titin molecules could contribute to disease induced by pathogenic *TTN* truncating variants. Similarly, it is tempting to hypothesize that mutations inducing cleavage of titin (e.g. through the generation of aberrant cleavage sites or by overactivation of endogenous proteases) could be a trigger of muscle disease. In this regard, titin has been shown to be the substrate of calpain-3 and MMP-2 proteases[14]. Similar to transgenic mice overexpressing full-length calpain-3[71], we find that AAV6-mediated MMP-2 expression in skeletal muscle is not enough to produce myopathy neither at 7 nor at 21 dpi (**Figure S10**). Accordingly, there is no evidence of titin cleavage in these experiments (**Figure S10A**). Our observations suggest that MMP-2 requires additional activation (e.g. through genetic mutations targeting autoinhibitory regions) to unleash its catalytic activity as reported in the cardiac setting[72-74]. Remarkably, considering the activation of calpain-3 we have detected in titin mKO muscles (**Figure 6D**), it is possible that titin cleavage by this protease can amplify the effects of TEVp on titin in TEVs-TTN muscles from 7 dpi.

In the past, a few titin KO mouse lines have been generated to model muscle disease. While systemic loss of titin is embryonically lethal, peri- or postnatal muscle-specific counterparts show phenotypes resembling those in our titin mKO samples, including sarcopenia and reduced muscle mass, internal myonuclei, sarcomeric disassembly and increased expression of titin interactors[10,11]. Hence, cessation of force transduction across titin appears to be sufficient to recapitulate structural and molecular anomalies in titin KO muscles. It is possible that disruption of sarcomere structure is a common contributor to the detected phenotypes. However, some alterations in homozygous titin mKO muscles at 3 dpi precede sarcomere disassembly, which is apparent only at ≥7 dpi. These early-onset phenotypes, which also occur in heterozygous titin mKO muscles despite the fact that sarcomere disruption is limited in this case, include mislocalization of desmin, myonuclei and mitochondria (**Figures 2-4, S4, S5**). We speculate that alteration of force-dependent interactions in slack titin may sustain these primordial effects even when sarcomere structure is preserved. Also, the fact that titin shows multimeric organization in sarcomeres[43,44] implies that tension on intact titin molecules may transiently increase as partner titins are cleaved. Hence, we cannot rule out the possibility that some extent of high-force titin mechanosensing is also triggered in mKO muscles. This effect could be particularly relevant in conditions where less than 50% titin molecules are cleaved, such as in heterozygous titin mKO muscles and in homozygous counterparts at 3 dpi. Indeed, the proportion of dysregulated genes in titin mKO muscles that are also dysregulated in *mdm* muscles is higher for heterozygous and 3 dpi homozygous samples (68 and 67%, respectively) than for 7 and 21 dpi counterparts (47 and 44%, respectively), which would agree with the expected high-force mechanosensing in deletion-bearing *mdm* titins[75] (**Figures 7C-E, S9D-F**).

Consistent with perturbed titin-based mechanosensing, in titin mKO samples we detect altered levels/activity of several titin interactors that modulate transcription or participate in protein quality control pathways (**Figure**

6, S7B). Remarkably, higher levels of M-line associated MuRF1 is the only change that we detect already at 3 dpi in homozygous titin mKO muscles, therefore preceding overt sarcomere and muscle mass loss. This result suggests that this titin-interacting ubiquitin ligase is a mediator of the myopathic response in targeted tissues. Supporting this scenario, overexpression of MuRF1 has been shown to cause muscle atrophy[76]. Future research is needed to understand how loss of force transmission across titin results in altered levels of titin interactors and the mechanistic links with the phenotypes present in titin mKO muscles. In this regard, further examination of whether MuRF1 inhibition can prevent the myopathic response induced by titin unloading will be highly informative. Our results in **Figure S8** indicate that current strategies to block MuRF1 that limit muscle atrophy in several settings[55-57] are not enough to prevent the MuRF1 upregulation nor the associated protein ubiquitination in homozygous titin mKO muscles, suggesting that more aggressive treatments may be required in this highly severe setting. Also, the fact that the worst of the mKO phenotypes are avoided at ~25% cleavage in TEVs-TTN heterozygous muscles at 7 dpi suggests that the effects of any given fraction of cleaved titin may be dependent on the zygosity of the targeted muscles, with potentially relevant mechanistic implications. Exploring this scenario will require titration of GFP-TEVp expression to ensure equivalent kinetics and extent of titin cleavage in both hetero and homozygous titin mKO muscles.

The development of gene KO technology in mice revolutionized functional genetics in mammals as it allowed to assess biological fitness of animals deprived of a single protein, in many instances uncovering the biological function of the targeted protein and its causative role in familial conditions[77]. However, KO approaches cannot be applied to scrutinize the mechanical roles of multifunctional proteins that must operate under tension. Our work demonstrates the use of TEV protease to achieve protein mKOs *in vivo*, i.e. ceased force transduction across the targeted protein with no alteration of protein levels. Taking into account enticing observations using optogenetics to mechanically knock out proteins *in vitro*[78,79], the protease-based strategy that we describe here could be exploited to dissect the complex functions of other mechanical proteins, including pathomechanisms of mutant proteins relevant for human disease such as dystrophin[4], nebulin[80], integrins[81], lamins[82], and cadherins[83]. Protease-based methods could also be extended to directly compare phenotypes of KO and mKO animals by tuning cleavage sites to couple proteolysis with degron activation[84].

Acknowledgements: JAC acknowledges funding from the European Research Council (ERC) under the European Union's Horizon 2020 research and innovation programme (grant agreement No. [101002927]). CNIC is supported by the Instituto de Salud Carlos III (ISCIII), the Ministerio de Ciencia, Innovación y Universidades (MCIU, MICIU/AEI/10.13039/501100011033) and the Pro CNIC Foundation, and is a Severo Ochoa Center of Excellence (grant CEX2020-001041-S funded by MCIU). ACD acknowledges funding from La Caixa Foundation (LCF/BQ/PI22/11910029) and the MCIU through project PID2022-140352NA-I00. RSR acknowledges funding from the European Molecular Biology Organization (EMBO, postdoctoral fellowship EMBO ALTF 417-2022). MGH is a PhD fellow from La Caixa Foundation (LCF/BQ/DR22/11950024), MIS

was awarded with a Welcome Trust fellowship (225914/Z/22/Z), JS and MALU acknowledge funding from MCIU (PRE2019-089130 and FJC2021-047055-I, respectively). We are deeply indebted to Prof. Siegfried Labeit for providing MyoMed205-spiked food and for advice setting up immunofluorescence experiments. CNIC Proteomics Unit acknowledge infrastructure funding by competitive grant EQC2021-007053-P funded by MCIU and by "European Union NextGenerationEU/PRTR". RNAseq experiments were performed in the Genomics Unit of the CNIC. Light microscopy was conducted at the CNIC Microscopy & Dynamic Imaging Unit. We thank ReDIB ICTS infrastructure TRIMA@CNIC (MCIN) funding for the Leica SP8 confocal microscope. Electron microscopy was conducted at the electron microscopy facility from Universidad Autónoma de Madrid with the help of Francisco Urbano-Olmos and Covadonga Aguado-Ballano. We acknowledge the personnel from CNIC animal housing, viral vectors, genomics, bioinformatics (especially to Lucía Sánchez-García), and histology facilities. We thank the personnel from the Histopathology Facility in Institut de Genétique et de Biologie Moléculaire et Celullaire (Illkirch, France), and Jorge Grasa (University of Zaragoza) and Matthew M. Borkowski (Aurora Scientific) for their help to set up 1200A Isolated Muscle Test apparatus. We acknowledge the feedback from many colleagues at CNIC, especially Joan Isern and Pura Muñoz-Cánoves. We thank all members of the Molecular Mechanics of the Cardiovascular System team for their support and input. We thank Cristina Morales and Alba Pobes-Lagartos for technical assistance. We thank three expert reviewers for their insightful feedback.

Author contributions: RSR, NV, DVC, EHG, MALU, MRP and JAC conceived and designed the experiments. RSR, NV, MGH, ACD, MGV and JAL executed and/or analyzed experiments. VLC, JS, OGS, MIS and JV contributed materials/analysis tools. RSR and JAC drafted the manuscript with input from all authors.

Declaration of interests: The authors declare no competing interests.

Methods

Animal experimentation

Mice were housed in ventilated cages with free access to food and water and 12h day/night cycles. Heterozygous TEVs-TTN animals were crossed to obtain WT, heterozygous and homozygous animals. We have described production and basal characterization of TEVs-TTN animals before[32]. 5´-TGCAGTACTGGAGTGTGAAGTATCC -3´ (exon 226), 5´-GAAACGTGTGAAGTATCAGGTTAGG-3´ (WT) and 5´-GAGCGATGCATCTATGTGTAGG -3´ (TEVs-TTN) primers were used for genotyping. For Pax7-lineage tracing experiments, heterozygous $Pax7^{CreERT}$ (JAX line #017763) and $Rosa26^{tdTomato}$ (JAX line #007914) were crossed with TEVs-TTN animals to generate homozygous TEVs-TTN animals heterozygous for $Pax7^{CreERT}$ and $Rosa26^{tdTomato}$. Only female mice were used for the experiments. All experimental procedures were done in accordance with Spanish and European legislation and approved by the institutional committee (project numbers PROEX 042/18 and PROEX 107.8/23). Treatment with MyoMed205-spiked food followed published protocols[85].

AAV6 production

AAV6 particles were produced by double transfection of HEK293T cells (ATCC) with plasmids containing adenovirus helper sequences together with rep (AAV2) and cap (AAV6) genes (PF0406, PlasmidFactory), and the pAAV plasmid encoding GFP-tagged uTEV3 protease under the cytomegalovirus (CMV) promoter[39] or N-terminal-HA-tagged MMP-2 under the MHCK7 promoter (Vector Builder). Cell lysates were treated with 150 U/mL Benzonase (Millipore) for 30 min at 37 °C and clarified by centrifugation. Viral particles were purified by iodixanol gradient ultracentrifugation using Polypropylene Optiseal tubes (361625, Beckman-Coulter), further concentrated using Amicon Ultra-15 tubes (100K MWCO, Millipore), and resuspended in PBS buffer supplemented with 0.001% pluronic F-68. Particle quantity was determined by real-time PCR targeting CMV promoter: ACCATGGTGATGCGGTTTTG (forward) and ATGGGGTGGAGACTTGGAAATC (reverse) primers. Titers are expressed as viral genomes per mL (vg/mL).

Intramuscular injection of AAV6

10 to 12-week-old female mice were anesthetized using ketamine/xylazine (100 mg/kg / 10 mg/kg) and injected with 1.5×10^{10} viral genomes/leg (resulting in infection of both EDL and TA muscles), or 25 µL of NaCl 0.9% as control. Mice were placed in a recovery machine until full recovery from anesthesia and placed back in their breeding cages until dissection. Mice were euthanized by CO_2 inhalation or by cervical dislocation. For lineage tracing experiments, AAV6 injection procedure was preceded by five consecutive days of intraperitoneal injections of 75 mg/kg tamoxifen diluted in corn oil, followed by a resting period of 10 days.

Protein expression analyses

A small piece of frozen muscle was weighed and placed in a TaKaRa® BioMasher Standard tube (9791A, Takara) with 40 µL of protein extraction buffer (50 mM Tris Buffer pH 6.8, 10 mM EGTA, 3% SDS, 50 mM N-ethylmaleimide) per mg of tissue. Muscles were homogenized using TaKaRa® BioMasher Standard microtube homogenizer (9790B, Takara), heated at 60ºC for 10 minutes and the soluble fraction was obtained by centrifugation at 18,000 g for 5 minutes at room temperature. To detect titin cleavage, the protein extract

was diluted with 4X bromophenol blue mix (0.3% bromophenol blue/50% glycerol) and loaded in 2% polyacrylamide / 0.5% agarose gels[86]. Gels were stained using Coomassie. For WB, protein extracts in 4X bromophenol blue mix were loaded in 12% polyacrylamide gels, transferred to nitrocellulose membranes and stained with primary and subsequent horseradish peroxidase-coupled secondary antibodies (antibodies are reported in the **Table S1**). Chemiluminiscence staining was performed using Amersham ECL Western Blotting Reagent (RPN2106, Cytiva). Membrane MemCode™ Reversible Protein Stain (24580, Thermo Scientific) was performed and imaged prior to antibody incubations and results were used for load normalization. For fingerprinting mass spectrometry, proteins were digested in-gel with trypsin (V5111)[87] and analyzed using an Evosep One chromatographic system (Evosep Biosystems) coupled with a Thermo Orbitrap Eclipse (Thermo Fisher) mass spectrometer, using a 21-min gradient separation and data-dependent MS/MS spectra. Protein identification was conducted using Sequest HT into Proteome Discoverer (Thermo Fisher). Identifications were validated based on probability thresholds and grouped according to the principles of parsimony by Scaffold software (Proteome Software).

Histology

Upon dissection, TA was frozen in liquid-nitrogen-cooled isopentane whereas EDL was fixed using 4% paraformaldehyde (PFA), cryopreserved in 30% sucrose, embedded in Tissue-Tek® (4583, Sakura) and frozen. For MuRF1, ANKRD1 and MMP-2 (HA tag) immunofluorescence, EDL was fixed using 40% methanol:40% acetic acid: 20% ultrapure water prior to sucrose treatment and embedding. 8-µm cryosections were permeabilized using 0.3% Triton X-100 (X100, Sigma), blocked with bovine serum albumin (A7906, Sigma) and stained with Alexa-coupled wheat germ agglutinin or with primary and secondary antibodies in the case of immunofluorescence (**Table S2**). Preparations were imaged on Nikon Eclipse 90i Timelapse (transverse TA sections) or Leica SP8 (longitudinal EDL sections) confocal microscopes. Full muscle transverse section images were recorded in Zeiss Axioscan 7 Scanner Microscopy (Zeiss).

Atomic Force Microscopy

Measurements were performed with a commercial JPK NanoWizard 4XP instrument (Bruker-JPK, Berlin, Germany) coupled to an inverted Axio Observer D1 optical microscope (Carl Zeiss, Germany). TA muscle cryosections with a thickness of 8 µm were probed at room temperature in PBS using CP-qp-CONT-SiO-A-5 cantilevers (Nanoandmore GmbH, Germany) with 2-µm-diameter colloidal spherical probes and pre-calibrated spring constant of 0.6 N m^{-1}. Force-distance (FD) curves were recorded in contact mode on the tissue surface to determine Young's moduli. Approach-retract cycles were performed with a tip velocity of 5 µm/s, a ramp size of 2 µm and a setpoint force of 5 nN, limiting the indentation to 0.8 µm. FD measurements were spread across at least three different areas of 100 x 100 μm^2 and several millimeters apart on each tissue sample. We analyzed between 150 and 500 FD curves per tissue sample. Young's modulus values (E) were calculated using the JPK Data Analysis software, by fitting the approach section of the curve to the Hertz[88] model for spherical indenters using Equation 1:

$$F = \frac{4}{3}\frac{E}{1-\nu^2}\sqrt{R\delta^3} \qquad \text{[Equation 1]}$$

In Equation 1, F is the applied force, R is the probe radius, ν is Poisson's ratio, and δ is the indentation. Tissues mostly consist of water and are considered incompressible, hence a Poisson ratio of 0.5 was chosen.

Ex vivo muscle force production

Mice were euthanized and EDL was isolated, tied using 5-0 silk suture thread (Fine Science Tools), and attached to a force transducer (1200A Isolated Muscle Test System, Aurora Scientific). EDL muscle was placed between platinum electrodes in a chamber continuously perfused with Ringer solution (137 mM NaCl, 5 mM KCl, 1.2 mM NaH_2PO_4, 1 mM $MgSO_4$, 2 mM $CaCl_2$, 10 mM glucose, and 24 mM $NaHCO_3$). Optimal muscle length was determined using 1 Hz twitches and finally adjusted using 100 Hz stimulations spaced by 1 minute. A force-frequency protocol consisting on stimulation trains of 0.5 seconds (1, 10, 20, 50, 80, 100, 120, 150 and 200 Hz) spaced by 1 minute was applied. Specific force was calculated by dividing the maximal force (mN) with the EDL cross sectional area calculated as wet muscle weight (mg)/optimal muscle length (mm) X mammalian muscle density (1.06 mg/mm^3).

Image analysis

WGA or HaloTMR-stained myofibers in histological sections were segmented using Cellpose 2.0[89]. Thresholds for GFP/necrosis/eMHC/desmin mislocalization were calculated within every experimental time point as these were stained, imaged and analyzed separately. For the analysis of myonuclei localization, additional segmentation of DAPI signal was performed using Fiji plugin StarDist[90]; assignment of their corresponding myofiber was calculated from myofiber ROI. Myonuclei distance to myofiber centroid was obtained. The ratio of distances of myonuclei and myofiber membrane to myofiber centroid was calculated according to:

$$Myonuclei\ distance\ ratio = \frac{Myonuclei\ to\ myofiber\ center\ distance}{Myofiber\ center\ to\ periphery\ distance} \qquad \text{[Equation 2]}$$

For the colocalization test of α-actinin, PEVK-Titin and cTEVsite, images of longitudinal EDL sections were first deconvolved using Huygens deconvolution software (Science Volume Imaging). Deconvolved images from 17-24 myofibers imaged in at least 3 different mice were used to obtain fluorescence signals across 73-106 sarcomeres, which were normalized and averaged at the α-actinin peak for every sarcomere. Counting of internal myonuclei on HE sections was performed manually using CellCounter ImageJ tool. Quantification of the degree of fibrosis was performed using a custom script written in ImageJ macro language and normalized with the contralateral leg in the same slide.

In vitro validation of cleaved TEV site (cTEVsite) antibody

The TEV protease and the recombinant fragment encompassing Ig86-TEVs-HaloTag-Ig87 were produced, and the proteolytic digestion performed as previously described[32]. We transferred the fragments to a nitrocellulose membrane and stained with a primary antibody targeting the TEV recognition site (NBP2-37831, Novus Biologicals) and peroxidase-coupled secondary targeting rabbit IgG (A0545, Sigma-Aldrich). In parallel, the products of digestion were also loaded in a dot blot transfer apparatus, where native proteins were air-vacuum-transferred into the nitrocellulose membrane and stained with primary and secondary antibodies as above. Total

protein staining with the Membrane MemCode Reversible Protein Stain (24580, Thermo Scientific) was performed and imaged prior to antibody incubations.

Electron microscopy

For electron microscopy EDL muscle was fixed in 2.5% glutaraldehyde, 2.5% PFA in 50 mM Cacodylate buffer (0.1M, pH 7.4) and postfixed in 1% osmium tetroxide for 60 minutes and dehydrated through a series of ethanol solutions (30%, 50%, 70%, 95%, 100%) and acetone. After the last dehydration step, samples were incubated consecutively in 1:3, 1:1, 3:1 DURCUPAN resin:acetone and cured at 60ºC for 48h. Ultrathin sections (50-60 nm) were obtained using a diamond knife (Diatome) in a Leica Reichert ultracut S ultramicrotome (Leica) and collected in microscope nickel grids (200 mesh). The sections were counterstained with 2% uranyl acetate in water for 20 min followed by a lead citrate solution for 10 minutes. They were examined with a JEM1010 electron microscope (JEOL) equipped with an Orius SC200 digital camera (Gatan Inc.).

Gene expression analysis

Muscles were lysed using Precellys homogenizing CK28 beads and Minilys homogenizer (Bertin technologies) using TRI Reagent (Sigma) and following manufacturer´s instructions. RNA quality was quantified using RNA Integrity Number (RIN) in a 2100 Bioanalyzer (Agilent Technologies) and next generation sequencing was performed with samples displaying RIN > 7. Total RNA (150 ng) was used to generate barcoded RNA-seq libraries using the NEBNext Ultra II Directional RNA Library preparation kit (New England Biolabs) according to manufacturer's instructions. First, poly A+ RNA was purified using oligo-dT- attached magnetic beads followed by fragmentation and first and second cDNA strand synthesis. Next, cDNA ends were repaired and adenylated. The NEBNext adaptor was then ligated followed by second strand removal, uracil excision from the adaptor and PCR amplification. The size of the libraries was checked using the Agilent 2100 Bioanalyzer and the concentration was determined using the Qubit® fluorometer (ThermoFisher). Libraries were sequenced at 650 pM on a NextSeq 2000 (Illumina) using a P3 flow cell to generate 50 bases paired-end reads. FastQ files for each sample were obtained using bcl2fastq v2 2.20 software (Illumina). RNAseq experiments were performed in the Genomics Unit of the CNIC. Sequencing reads were pre-processed by a pipeline that used FastQC (http://www.bioinformatics.babraham.ac.uk/projects/fastqc/) to assess read quality, and Cutadapt[91] to remove adaptor remains from Illumina and to discard reads that were shorter than 30 bp. The resulting reads were mapped against reference transcriptome GRCm38.99 and quantified with RSEM[92], using Bowtie as aligner. The expected expression counts calculated with RSEM were processed with a pipeline that used Limma package[93], from Bioconductor, for normalization and differential expression testing, taking only into account those genes expressed with at least 1 count per million (CPM) in at least three samples. Changes in gene expression were considered significant if associated to Benjamini and Hochberg adjusted p-value < 0.05 and absolute log2 fold change higher than 0.5 and lower than -0.5. Functional enrichment analyses were performed with Gene Set Enrichment Analysis of pathways comprising more than 15 and less than 500 genes (GSEA)[94]. Graphical representations (PCA plots, heatmaps) were generated with R. For comparison of the genes differentially expressed in titin mKO and mdm[59] muscles, data were reanalysed using Galaxy web platform

tools[95] including alignment (STAR), expression counts (featureCounts) and differences in gene expression (DESeq2). The gene ontology enrichment of commonly dysregulated genes in the 2 lines was calculated using PANTHER[96]. Accession codes are GSE271916 (GEO private token sbazceucbxavdkt) for the RNAseq data of TEVs-TTN mice and GSE158283 and GSE210263 for mdm mice[59].

Statistical analysis and preparation of figures

All experiments were performed and analyzed in a blinded manner, and the investigators were unaware of the genotype of the mice. Data are presented as mean ± standard error of the mean (SEM). Normal distribution of data was assessed using the Shapiro-Wilk test. For normally distributed data, the significance of changes was examined by two-tailed Student's t test for comparison of 2 groups or by one-way ANOVA followed by Tukey's post hoc test for comparison of more than 2 groups. In the case of not-normally distributed data, the Mann-Whitney test was used to compare 2 groups. Significant differences are illustrated as $*p < 0.05$, $**p < 0.01$, $***p < 0.001$ and $****p < 0.0001$. Statistical analyses were performed using GraphPad Prism (GraphPad) and tests were two-sided. Figures have been generated using GrahPad Prism 10, Adobe Illustrator, BioRender.com for Figures 1A, 1B, 1H, 1K, 5A and 5H.

Data availability

The main data supporting the results in this study are available within the paper and its Supplementary Information. Non-commercial materials are available from the corresponding authors. Transcriptomic data from bulk RNA-seq are available from the Gene Expression Omnibus (GEO) with GSE271916 accession code (GEO private token sbazceucbxavdkt) and transcriptomic data of EDL and psoas muscles was obtained from GSE158283[59] and GSE210263[59].

References

1 Klapholz, B. & Brown, N. H. Talin - the master of integrin adhesions. *J Cell Sci* **130**, 2435-2446 (2017). https://doi.org/10.1242/jcs.190991

2 Leckband, D. E. & de Rooij, J. Cadherin adhesion and mechanotransduction. *Annu Rev Cell Dev Biol* **30**, 291-315 (2014). https://doi.org/10.1146/annurev-cellbio-100913-013212

3 Gruenbaum, Y. & Foisner, R. Lamins: nuclear intermediate filament proteins with fundamental functions in nuclear mechanics and genome regulation. *Annu Rev Biochem* **84**, 131-164 (2015). https://doi.org/10.1146/annurev-biochem-060614-034115

4 Wilson, D. G. S., Tinker, A. & Iskratsch, T. The role of the dystrophin glycoprotein complex in muscle cell mechanotransduction. *Commun Biol* **5**, 1022 (2022). https://doi.org/10.1038/s42003-022-03980-y

5 Brynnel, A., Hernandez, Y., . . . Granzier, H. L. Downsizing the molecular spring of the giant protein titin reveals that skeletal muscle titin determines passive stiffness and drives longitudinal hypertrophy. *Elife* **7** (2018). https://doi.org/10.7554/eLife.40532

6 Buck, D., Smith, J. E., 3rd, . . . Granzier, H. L. Removal of immunoglobulin-like domains from titin's spring segment alters titin splicing in mouse skeletal muscle and causes myopathy. *J Gen Physiol* **143**, 215-230 (2014). https://doi.org/10.1085/jgp.201311129

7 Chung, C. S., Hutchinson, K. R., . . . Granzier, H. L. Shortening of the elastic tandem immunoglobulin segment of titin leads to diastolic dysfunction. *Circulation* **128**, 19-28 (2013). https://doi.org/10.1161/CIRCULATIONAHA.112.001268

8 Granzier, H. L., Radke, M. H., . . . Gotthardt, M. Truncation of titin's elastic PEVK region leads to cardiomyopathy with diastolic dysfunction. *Circ Res* **105**, 557-564 (2009). https://doi.org/10.1161/CIRCRESAHA.109.200964

9 Radke, M. H., Peng, J., . . . Gotthardt, M. Targeted deletion of titin N2B region leads to diastolic dysfunction and cardiac atrophy. *Proc Natl Acad Sci U S A* **104**, 3444-3449 (2007). https://doi.org/10.1073/pnas.0608543104

10 Radke, M. H., Polack, C., . . . Gotthardt, M. Deleting Full Length Titin Versus the Titin M-Band Region Leads to Differential Mechanosignaling and Cardiac Phenotypes. *Circulation* **139**, 1813-1827 (2019). https://doi.org/10.1161/CIRCULATIONAHA.118.037588

11 Swist, S., Unger, A., . . . Linke, W. A. Maintenance of sarcomeric integrity in adult muscle cells crucially depends on Z-disc anchored titin. *Nat Commun* **11**, 4479 (2020). https://doi.org/10.1038/s41467-020-18131-2

12 Alegre-Cebollada, J. Protein nanomechanics in biological context. *Biophys Rev* **13**, 435-454 (2021). https://doi.org/10.1007/s12551-021-00822-9

13 Granzier, H. L. & Labeit, S. Discovery of Titin and Its Role in Heart Function and Disease. *Circ Res* **136**, 135-157 (2025). https://doi.org/10.1161/CIRCRESAHA.124.323051

14 Linke, W. A. & Hamdani, N. Gigantic business: titin properties and function through thick and thin. *Circulation Research* **114**, 1052-1068 (2014). https://doi.org/10.1161/CIRCRESAHA.114.301286

15 Saucerman, J. J., Tan, P. M., . . . Omens, J. H. Mechanical regulation of gene expression in cardiac myocytes and fibroblasts. *Nat Rev Cardiol* **16**, 361-378 (2019). https://doi.org/10.1038/s41569-019-0155-8

16 Kotter, S., Unger, A., . . . Linke, W. A. Human myocytes are protected from titin aggregation-induced stiffening by small heat shock proteins. *J Cell Biol* **204**, 187-202 (2014). https://doi.org/10.1083/jcb.201306077

17 Sun, Y., Liu, X., . . . Yan, J. Structural domain in the Titin N2B-us region binds to FHL2 in a force-activation dependent manner. *Nat Commun* **15**, 4496 (2024). https://doi.org/10.1038/s41467-024-48828-7

18 Bogomolovas, J., Fleming, J. R., . . . Mayans, O. Titin kinase ubiquitination aligns autophagy receptors with mechanical signals in the sarcomere. *EMBO Rep* **22**, e48018 (2021). https://doi.org/10.15252/embr.201948018

19 Bogomolovas, J., Gasch, A., . . . Mayans, O. Titin kinase is an inactive pseudokinase scaffold that supports MuRF1 recruitment to the sarcomeric M-line. *Open Biol* **4**, 140041 (2014). https://doi.org/10.1098/rsob.140041
20 Lange, S., Xiang, F., . . . Gautel, M. The kinase domain of titin controls muscle gene expression and protein turnover. *Science* **308**, 1599-1603 (2005). https://doi.org/10.1126/science.1110463
21 Puchner, E. M., Alexandrovich, A., . . . Gautel, M. Mechanoenzymatics of titin kinase. *Proc Natl Acad Sci U S A* **105**, 13385-13390 (2008). https://doi.org/10.1073/pnas.0805034105
22 Alegre-Cebollada, J., Kosuri, P., . . . Fernandez, J. M. S-glutathionylation of cryptic cysteines enhances titin elasticity by blocking protein folding. *Cell* **156**, 1235-1246 (2014). https://doi.org/10.1016/j.cell.2014.01.056
23 Herman, D. S., Lam, L., . . . Seidman, C. E. Truncations of titin causing dilated cardiomyopathy. *N Engl J Med* **366**, 619-628 (2012). https://doi.org/10.1056/NEJMoa1110186
24 Oates, E. C., Jones, K. J., . . . Laing, N. G. Congenital Titinopathy: Comprehensive characterization and pathogenic insights. *Annals of Neurology* **83**, 1105-1124 (2018). https://doi.org/10.1002/ana.25241
25 Savarese, M., Sarparanta, J., . . . Hackman, P. Increasing Role of Titin Mutations in Neuromuscular Disorders. *Journal of Neuromuscular Disorders* **3**, 293-308 (2016). https://doi.org/10.3233/JND-160158
26 Savarese, M., Vihola, A., . . . Udd, B. Genotype-phenotype correlations in recessive titinopathies. *Genetics in Medicine* **22**, 2029-2040 (2020). https://doi.org/10.1038/s41436-020-0914-2
27 Hinson, J. T. & Campbell, S. G. TTN truncation variants produce sarcomere-integrating proteins of uncertain functional significance. *J Clin Invest* **134** (2024). https://doi.org/10.1172/JCI175206
28 Kellermayer, D., Tordai, H., . . . Kellermayer, M. S. Truncated titin is structurally integrated into the human dilated cardiomyopathic sarcomere. *J Clin Invest* **134** (2024). https://doi.org/10.1172/JCI169753
29 McAfee, Q., Caporizzo, M. A., . . . Prosser, B. L. Truncated titin protein in dilated cardiomyopathy incorporates into the sarcomere and transmits force. *J Clin Invest* **134** (2024). https://doi.org/10.1172/JCI170196
30 Horowits, R., Kempner, E. S., . . . Podolsky, R. J. A physiological role for titin and nebulin in skeletal muscle. *Nature* **323**, 160-164 (1986). https://doi.org/10.1038/323160a0
31 Li, Y., Hessel, A. L., . . . Linke, W. A. Graded titin cleavage progressively reduces tension and uncovers the source of A-band stability in contracting muscle. *Elife* **9** (2020). https://doi.org/10.7554/eLife.64107
32 Rivas-Pardo, J. A., Li, Y., . . . Alegre-Cebollada, J. A HaloTag-TEV genetic cassette for mechanical phenotyping of proteins from tissues. *Nature Communications* **11**, 2060 (2020). https://doi.org/10.1038/s41467-020-15465-9
33 Loescher, C. M., Freundt, J. K., . . . Linke, W. A. Titin governs myocardial passive stiffness with major support from microtubules and actin and the extracellular matrix. *Nat Cardiovasc Res* **2**, 991-1002 (2023). https://doi.org/10.1038/s44161-023-00348-1
34 Rivas-Pardo, J. A., Li, Y., . . . Alegre-Cebollada, J. A HaloTag-TEV genetic cassette for mechanical phenotyping of proteins from tissues. *Nat Commun* **11**, 2060 (2020). https://doi.org/10.1038/s41467-020-15465-9
35 Hessel, A. L., Kuehn, M. N., . . . Linke, W. A. Titin-Based Force Modulates Cardiac Thick and Thin Filaments. *Circ Res* **134**, 1026-1028 (2024). https://doi.org/10.1161/CIRCRESAHA.123.323988
36 Hessel, A. L., Kuehn, M. N., . . . Linke, W. A. The distinctive mechanical and structural signatures of residual force enhancement in myofibers. *Proc Natl Acad Sci U S A* **121**, e2413883121 (2024). https://doi.org/10.1073/pnas.2413883121
37 Hessel, A. L., Ma, W., . . . Linke, W. A. Titin force in muscle cells alters lattice order, thick and thin filament protein formation. *Proc Natl Acad Sci U S A* **119**, e2209441119 (2022). https://doi.org/10.1073/pnas.2209441119

38 Douvdevany, G., Erlich, I., . . . Kehat, I. Imaging of Existing and Newly Translated Proteins Elucidates Mechanisms of Sarcomere Turnover. *Circ Res* **135**, 474-487 (2024). https://doi.org/10.1161/CIRCRESAHA.123.323819

39 Sanchez, M. I. & Ting, A. Y. Directed evolution improves the catalytic efficiency of TEV protease. *Nat Methods* **17**, 167-174 (2020). https://doi.org/10.1038/s41592-019-0665-7

40 Rodrigues, M., Echigoya, Y., . . . Yokota, T. Impaired regenerative capacity and lower revertant fibre expansion in dystrophin-deficient mdx muscles on DBA/2 background. *Sci Rep* **6**, 38371 (2016). https://doi.org/10.1038/srep38371

41 Wells, K. E., Maule, J., . . . Wells, D. J. Immune responses, not promoter inactivation, are responsible for decreased long-term expression following plasmid gene transfer into skeletal muscle. *FEBS Lett* **407**, 164-168 (1997). https://doi.org/10.1016/s0014-5793(97)00329-3

42 Hnia, K., Tronchere, H., . . . Laporte, J. Myotubularin controls desmin intermediate filament architecture and mitochondrial dynamics in human and mouse skeletal muscle. *J Clin Invest* **121**, 70-85 (2011). https://doi.org/10.1172/JCI44021

43 Dutta, D., Nguyen, V., . . . Craig, R. Cryo-EM structure of the human cardiac myosin filament. *Nature* **623**, 853-862 (2023). https://doi.org/10.1038/s41586-023-06691-4

44 Tamborrini, D., Wang, Z., . . . Raunser, S. Structure of the native myosin filament in the relaxed cardiac sarcomere. *Nature* **623**, 863-871 (2023). https://doi.org/10.1038/s41586-023-06690-5

45 Li, H., Linke, W. A., . . . Fernandez, J. M. Reverse engineering of the giant muscle protein titin. *Nature* **418**, 998-1002 (2002). https://doi.org/10.1038/nature00938

46 Madisen, L., Zwingman, T. A., . . . Zeng, H. A robust and high-throughput Cre reporting and characterization system for the whole mouse brain. *Nat Neurosci* **13**, 133-140 (2010). https://doi.org/10.1038/nn.2467

47 Murphy, M. M., Lawson, J. A., . . . Kardon, G. Satellite cells, connective tissue fibroblasts and their interactions are crucial for muscle regeneration. *Development* **138**, 3625-3637 (2011). https://doi.org/10.1242/dev.064162

48 Laure, L., Suel, L., . . . Daniele, N. Cardiac ankyrin repeat protein is a marker of skeletal muscle pathological remodelling. *FEBS J* **276**, 669-684 (2009). https://doi.org/10.1111/j.1742-4658.2008.06814.x

49 van der Pijl, R. J., van den Berg, M., . . . Ottenheijm, C. A. C. Muscle ankyrin repeat protein 1 (MARP1) locks titin to the sarcomeric thin filament and is a passive force regulator. *J Gen Physiol* **153**, e202112925 (2021). https://doi.org/10.1085/jgp.202112925

50 Zhou, T., Fleming, J. R., . . . Mayans, O. Molecular Characterisation of Titin N2A and Its Binding of CARP Reveals a Titin/Actin Cross-linking Mechanism. *J Mol Biol* **433**, 166901 (2021). https://doi.org/10.1016/j.jmb.2021.166901

51 Laure, L., Daniele, N., . . . Richard, I. A new pathway encompassing calpain 3 and its newly identified substrate cardiac ankyrin repeat protein is involved in the regulation of the nuclear factor-kappaB pathway in skeletal muscle. *FEBS J* **277**, 4322-4337 (2010). https://doi.org/10.1111/j.1742-4658.2010.07820.x

52 Willis, M. S., Ike, C., . . . Patterson, C. Muscle ring finger 1, but not muscle ring finger 2, regulates cardiac hypertrophy in vivo. *Circ Res* **100**, 456-459 (2007). https://doi.org/10.1161/01.RES.0000259559.48597.32

53 Willis, M. S., Rojas, M., . . . Patterson, C. Muscle ring finger 1 mediates cardiac atrophy in vivo. *Am J Physiol Heart Circ Physiol* **296**, H997-H1006 (2009). https://doi.org/10.1152/ajpheart.00660.2008

54 Cowling, B. S., McGrath, M. J., . . . Mitchell, C. A. Identification of FHL1 as a regulator of skeletal muscle mass: implications for human myopathy. *J Cell Biol* **183**, 1033-1048 (2008). https://doi.org/10.1083/jcb.200804077

55 Adams, V., Schauer, A., . . . Labeit, S. Targeting MuRF1 by small molecules in a HFpEF rat model improves myocardial diastolic function and skeletal muscle contractility. *J Cachexia Sarcopenia Muscle* **13**, 1565-1581 (2022). https://doi.org/10.1002/jcsm.12968

56 Ribeiro, F., Alves, P. K. N., . . . Moriscot, A. S. Small-Molecule Inhibition of MuRF1 Prevents Early Disuse-Induced Diaphragmatic Dysfunction and Atrophy. *Int J Mol Sci* **24** (2023). https://doi.org/10.3390/ijms24043637

57 Adams, V., Gussen, V., . . . Labeit, S. Small-Molecule Chemical Knockdown of MuRF1 in Melanoma Bearing Mice Attenuates Tumor Cachexia Associated Myopathy. *Cells* **9** (2020). https://doi.org/10.3390/cells9102272

58 Mootha, V. K., Lindgren, C. M., . . . Groop, L. C. PGC-1alpha-responsive genes involved in oxidative phosphorylation are coordinately downregulated in human diabetes. *Nat Genet* **34**, 267-273 (2003). https://doi.org/10.1038/ng1180

59 Hettige, P., Tahir, U., . . . Gage, M. J. Transcriptomic profiles of muscular dystrophy with myositis (mdm) in extensor digitorum longus, psoas, and soleus muscles from mice. *BMC Genomics* **23**, 657 (2022). https://doi.org/10.1186/s12864-022-08873-2

60 Roman, W., Martins, J. P., . . . Gomes, E. R. Myofibril contraction and crosslinking drive nuclear movement to the periphery of skeletal muscle. *Nat Cell Biol* **19**, 1189-1201 (2017). https://doi.org/10.1038/ncb3605

61 Hackman, P., Vihola, A., . . . Udd, B. Tibial muscular dystrophy is a titinopathy caused by mutations in TTN, the gene encoding the giant skeletal-muscle protein titin. *Am J Hum Genet* **71**, 492-500 (2002). https://doi.org/10.1086/342380

62 Partanen, J., Laulumaa, V., . . . Naukkarinen, A. Late onset foot-drop muscular dystrophy with rimmed vacuoles. *J Neurol Sci* **125**, 158-167 (1994). https://doi.org/10.1016/0022-510x(94)90029-9

63 Udd, B., Kaarianen, H. & Somer, H. Muscular dystrophy with separate clinical phenotypes in a large family. *Muscle Nerve* **14**, 1050-1058 (1991). https://doi.org/10.1002/mus.880141103

64 Udd, B., Vihola, A., . . . Hackman, P. Titinopathies and extension of the M-line mutation phenotype beyond distal myopathy and LGMD2J. *Neurology* **64**, 636-642 (2005). https://doi.org/10.1212/01.WNL.0000151853.50144.82

65 De Cid, R., Ben Yaou, R., . . . Richard, I. A new titinopathy: Childhood-juvenile onset Emery-Dreifuss-like phenotype without cardiomyopathy. *Neurology* **85**, 2126-2135 (2015). https://doi.org/10.1212/WNL.0000000000002200

66 Chinnery, P. F., Johnson, M. A., . . . Bushby, K. M. A novel autosomal dominant distal myopathy with early respiratory failure: clinico-pathologic characteristics and exclusion of linkage to candidate genetic loci. *Ann Neurol* **49**, 443-452 (2001).

67 Pfeffer, G., Elliott, H. R., . . . Chinnery, P. F. Titin mutation segregates with hereditary myopathy with early respiratory failure. *Brain* **135**, 1695-1713 (2012). https://doi.org/10.1093/brain/aws102

68 Ceyhan-Birsoy, O., Agrawal, P. B., . . . Beggs, A. H. Recessive truncating titin gene, TTN, mutations presenting as centronuclear myopathy. *Neurology* **81**, 1205-1214 (2013). https://doi.org/10.1212/WNL.0b013e3182a6ca62

69 Chauveau, C., Bonnemann, C. G., . . . Ferreiro, A. Recessive TTN truncating mutations define novel forms of core myopathy with heart disease. *Hum Mol Genet* **23**, 980-991 (2014). https://doi.org/10.1093/hmg/ddt494

70 Haggerty, C. M., Damrauer, S. M., . . . Arany, Z. Genomics-First Evaluation of Heart Disease Associated With Titin-Truncating Variants. *Circulation* **140**, 42-54 (2019). https://doi.org/10.1161/CIRCULATIONAHA.119.039573

71 Spencer, M. J., Guyon, J. R., . . . Beckmann, J. S. Stable expression of calpain 3 from a muscle transgene in vivo: immature muscle in transgenic mice suggests a role for calpain 3 in muscle maturation. *Proc Natl Acad Sci U S A* **99**, 8874-8879 (2002). https://doi.org/10.1073/pnas.132269299

72 Ali, M. A., Cho, W. J., . . . Schulz, R. Titin is a target of matrix metalloproteinase-2: implications in myocardial ischemia/reperfusion injury. *Circulation* **122**, 2039-2047 (2010). https://doi.org/10.1161/CIRCULATIONAHA.109.930222

73 Bergman, M. R., Teerlink, J. R., . . . Lovett, D. H. Cardiac matrix metalloproteinase-2 expression independently induces marked ventricular remodeling and systolic dysfunction. *Am J Physiol Heart Circ Physiol* **292**, H1847-1860 (2007). https://doi.org/10.1152/ajpheart.00434.2006

74 Viappiani, S., Nicolescu, A. C., . . . Schulz, R. Activation and modulation of 72kDa matrix metalloproteinase-2 by peroxynitrite and glutathione. *Biochem Pharmacol* **77**, 826-834 (2009). https://doi.org/10.1016/j.bcp.2008.11.004
75 Garvey, S. M., Rajan, C., . . . Cox, G. A. The muscular dystrophy with myositis (mdm) mouse mutation disrupts a skeletal muscle-specific domain of titin. *Genomics* **79**, 146-149 (2002). https://doi.org/10.1006/geno.2002.6685
76 Baehr, L. M., Hughes, D. C., . . . Bodine, S. C. Identification of the MuRF1 Skeletal Muscle Ubiquitylome Through Quantitative Proteomics. *Function (Oxf)* **2**, zqab029 (2021). https://doi.org/10.1093/function/zqab029
77 Austin, C. P., Battey, J. F., . . . Zambrowicz, B. The knockout mouse project. *Nat Genet* **36**, 921-924 (2004). https://doi.org/10.1038/ng0904-921
78 Endo, M., Iwawaki, T., . . . Ozawa, T. Photocleavable Cadherin Inhibits Cell-to-Cell Mechanotransduction by Light. *ACS Chem Biol* **14**, 2206-2214 (2019). https://doi.org/10.1021/acschembio.9b00460
79 Sadhanasatish, T., Augustin, K., . . . Grashoff, C. A molecular optomechanics approach reveals functional relevance of force transduction across talin and desmoplakin. *Sci Adv* **9**, eadg3347 (2023). https://doi.org/10.1126/sciadv.adg3347
80 Labeit, S., Ottenheijm, C. A. & Granzier, H. Nebulin, a major player in muscle health and disease. *FASEB J* **25**, 822-829 (2011). https://doi.org/10.1096/fj.10-157412
81 Wickstrom, S. A., Radovanac, K. & Fassler, R. Genetic analyses of integrin signaling. *Cold Spring Harb Perspect Biol* **3** (2011). https://doi.org/10.1101/cshperspect.a005116
82 Schreiber, K. H. & Kennedy, B. K. When lamins go bad: nuclear structure and disease. *Cell* **152**, 1365-1375 (2013). https://doi.org/10.1016/j.cell.2013.02.015
83 El-Amraoui, A. & Petit, C. Cadherins as targets for genetic diseases. *Cold Spring Harb Perspect Biol* **2**, a003095 (2010). https://doi.org/10.1101/cshperspect.a003095
84 Taxis, C., Stier, G., . . . Knop, M. Efficient protein depletion by genetically controlled deprotection of a dormant N-degron. *Mol Syst Biol* **5**, 267 (2009). https://doi.org/10.1038/msb.2009.25
85 Alves, P. K. N., Cruz, A., . . . Labeit, S. Small-molecule mediated MuRF1 inhibition protects from doxorubicin-induced cardiac atrophy and contractile dysfunction. *Eur J Pharmacol* **984**, 177027 (2024). https://doi.org/10.1016/j.ejphar.2024.177027
86 Unger, A., Beckendorf, L., . . . Linke, W. A. Translocation of molecular chaperones to the titin springs is common in skeletal myopathy patients and affects sarcomere function. *Acta Neuropathol Commun* **5**, 72 (2017). https://doi.org/10.1186/s40478-017-0474-0
87 Martin-Cofreces, N. B., Chichon, F. J., . . . Sanchez-Madrid, F. The chaperonin CCT controls T cell receptor-driven 3D configuration of centrioles. *Sci Adv* **6** (2020). https://doi.org/10.1126/sciadv.abb7242
88 Schillers, H., Rianna, C., . . . Radmacher, M. Standardized Nanomechanical Atomic Force Microscopy Procedure (SNAP) for Measuring Soft and Biological Samples. *Sci Rep* **7**, 5117 (2017). https://doi.org/10.1038/s41598-017-05383-0
89 Pachitariu, M. & Stringer, C. Cellpose 2.0: how to train your own model. *Nat Methods* **19**, 1634-1641 (2022). https://doi.org/10.1038/s41592-022-01663-4
90 Schmidt, U., Weigert, M., . . . Myers, G. 265-273 (Springer International Publishing).
91 Martin, M. Cutadapt removes adapter sequences from high-throughput sequencing reads. *2011* **17**, 3 (2011). https://doi.org/10.14806/ej.17.1.200
92 Li, B. & Dewey, C. N. RSEM: accurate transcript quantification from RNA-Seq data with or without a reference genome. *BMC Bioinformatics* **12**, 323 (2011). https://doi.org/10.1186/1471-2105-12-323
93 Ritchie, M. E., Phipson, B., . . . Smyth, G. K. limma powers differential expression analyses for RNA-sequencing and microarray studies. *Nucleic Acids Res* **43**, e47 (2015). https://doi.org/10.1093/nar/gkv007
94 Subramanian, A., Tamayo, P., . . . Mesirov, J. P. Gene set enrichment analysis: a knowledge-based approach for interpreting genome-wide expression profiles. *Proceedings of the National Academy of*

Sciences of the United States of America **102**, 15545-15550 (2005). https://doi.org/10.1073/pnas.0506580102

95 Galaxy, C. The Galaxy platform for accessible, reproducible, and collaborative data analyses: 2024 update. *Nucleic Acids Research* (2024). https://doi.org/10.1093/nar/gkae410

96 Mi, H., Muruganujan, A., . . . Thomas, P. D. Protocol Update for large-scale genome and gene function analysis with the PANTHER classification system (v.14.0). *Nature Protocols* **14**, 703-721 (2019). https://doi.org/10.1038/s41596-019-0128-8

804 # Figures

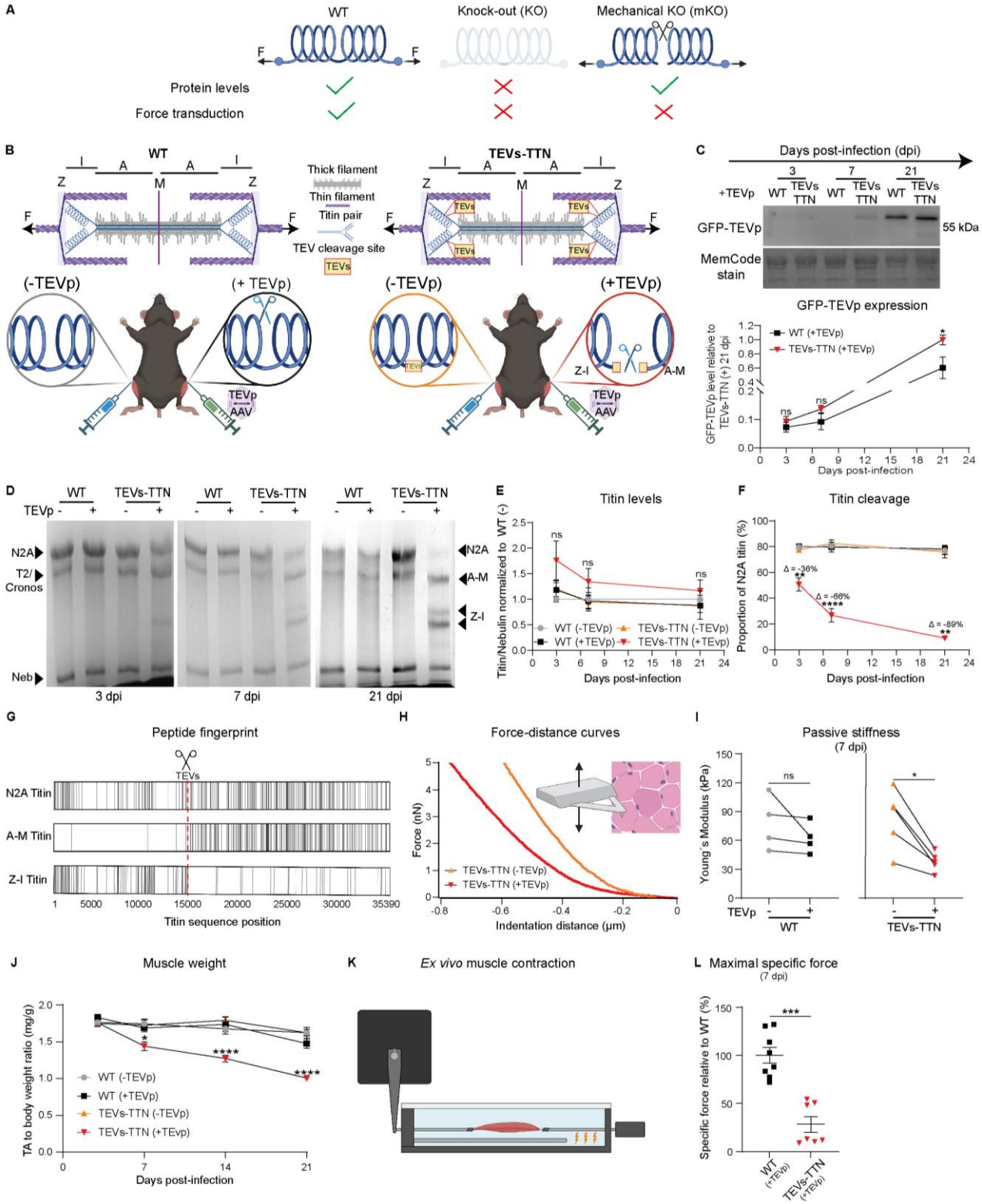

Figure 1. Titin mKO induces muscle atrophy and reduced force generation. (A) Conceptual comparison of traditional KO and mKO strategies to study a mechanical protein. A mKO achieves loss of force transmission across the targeted protein without affecting its expression levels. **(B)** Scheme of experimental setup. WT and TEVs-TTN legs are injected either with vehicle saline buffer (-TEVp, blue) or AAV6-GFP-TEVp (+TEVp, green). Representations of sarcomeres are shown. Titin cleavage can only occur in AAV6-GFP-TEVp injected TEVs-TTN muscles. Insets indicate the region of I-band titin where the TEV recognition site (yellow box) is inserted in TEVs-TTN mice. Titin fragments resulting from TEVp activity are indicated. **(C)** GFP-TEVp expression measured by WB using anti-GFP antibody.

MemCode staining was used as loading control (n=5-6). **(D)** Titin integrity measured on Coomassie-stained 2% acrylamide SDS-PAGE gels. Position of detected titin and nebulin bands are indicated. **(E)** Total titin levels (sum of all titin bands). Nebulin was used for normalization (n=2-6). **(F)** Quantification of proportion of N2A with respect to all titin bands (n=3-6). **(G)** Position of identified peptides in mass-spectrometry experiments (at 1% false discovery rate) using the indicated titin bands (N2A band coming from a contralateral-vehicle-injected TEVs-TTN sample). The position of the TEV recognition site is indicated by a dashed line. **(H)** Cartoon representing mechanical characterization of TA muscle cryosections using atomic force microscopy, and representative indentation traces. **(I)** Young's moduli of TA myofibers obtained using AFM at 7 dpi. (-TEVp) and (+TEVp) data points coming from the same animal are paired (n=4-5). **(J)** TA muscle weight to body weight ratio (n=4-14). **(K)** Scheme of *ex vivo* muscle mechanical characterization. **(L)** Maximal specific active force produced by AAV6-injected EDL muscles at 7 dpi (n=7-8). Data are represented as mean ± SEM.

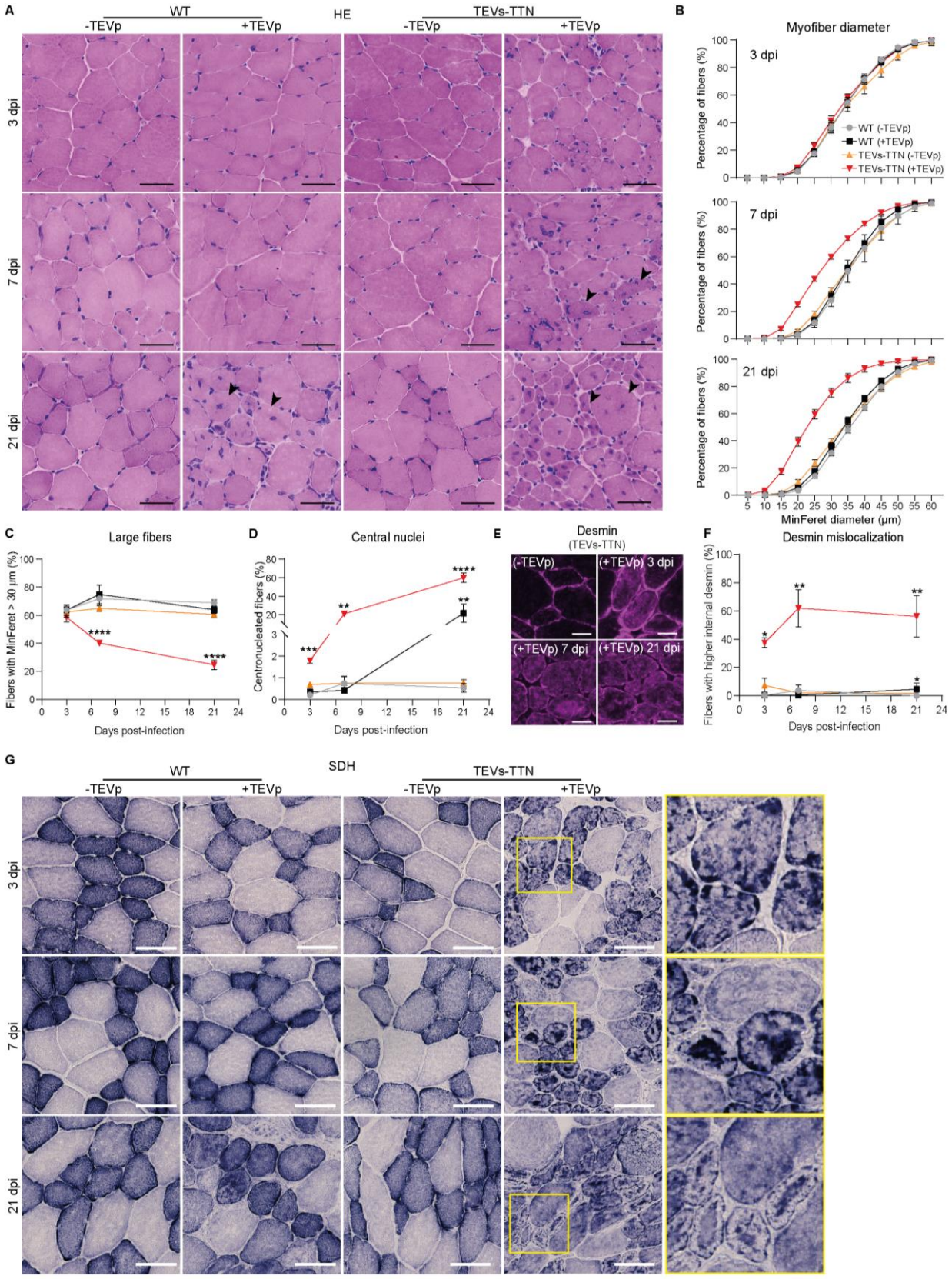

Figure 2. Histopathology of titin mKO muscles. (A) HE stainings of TA muscle. Black arrowheads indicate myofibers with centralized myonuclei. Scale bars represent 50 µm. **(B)** Distribution of the MinFeret diameter of myofibers measured using WGA stainings in **Figure S1A**.**(C,D)** Time evolution of the fraction of myofibers with MinFeret diameter larger than 30 µm (C) or centralized myonuclei (D) (n=3-6). **(E)** Desmin staining in transverse TA muscle sections. Scale bars represent 20 µm. **(F)** Fraction of myofibers with increased sarcoplasmic desmin

staining (n=3-5). **(G)** SDH mitochondrial activity staining of TA muscles (n=5). Color legends are indicated in insert in panel B. Scale bars represent 50 µm. Data are represented as mean ± SEM.

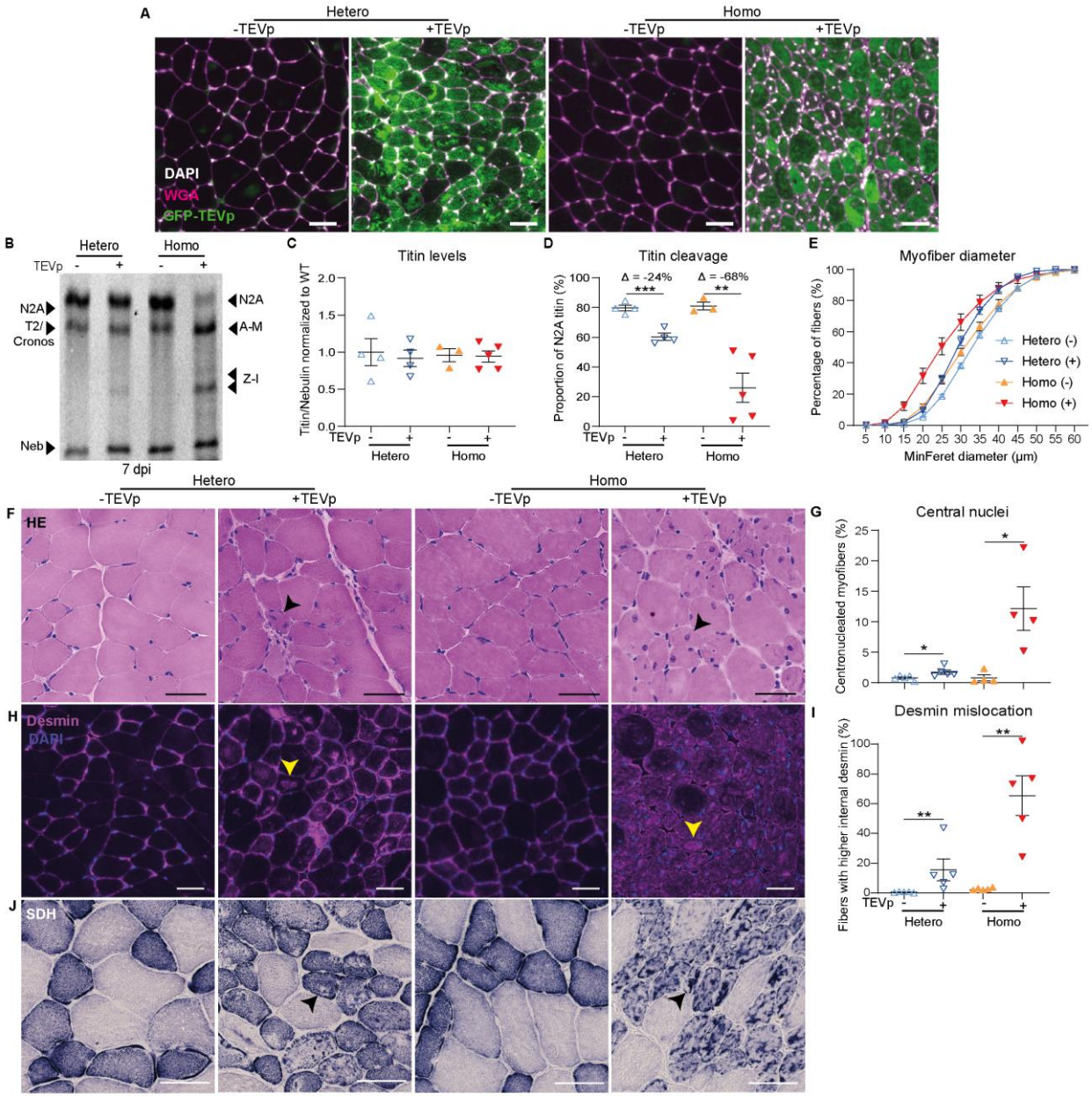

Figure 3. Intermediate phenotypes in heterozygous titin mKO muscles. (A) Immunofluorescence using WGA and anti-GFP antibodies of homozygous and heterozygous TEVs-TTN muscles at 7 dpi. Scale bars represent 50 µm. **(B)** Titin integrity measured on Coomassie-stained 2% acrylamide SDS-PAGE gels. Position of detected titin bands are indicated. **(C)** Total titin levels (sum of all titin bands). Nebulin was used for normalization (n=4-5). **(D)** Quantification of proportion of N2A with respect to all titin bands (n=4-5). **(E)** Distribution of myofiber MinFeret diameter measured in WGA immunofluorescence (n=9-10). **(F)** HE staining of homozygous and heterozygous TEVs-TTN muscles at 7 dpi. Arrowheads mark myofibers with central myonuclei. Scale bars represent 50 µm. **(G)** Fraction of myofibers with central myonuclei measured in HE staining (n=4-5). **(H)** Immunofluorescence to visualize desmin in homozygous and heterozygous TEVs-TTN muscles at 7 dpi. Arrowheads mark selected myofibers showing desmin mislocalization. Scale bars represent 50 µm. **(I)** Fraction of myofibers with mislocalized desmin (n=5). **(J)** SDH staining on transverse TA sections of heterozygous and homozygous TEVs-TTN muscles. Arrowheads mark myofibers with cores in heterozygous muscle and mitochondrial aggregation in homozygous muscle. Scale bars represent 50 µm. Data are represented as mean ± SEM.

806

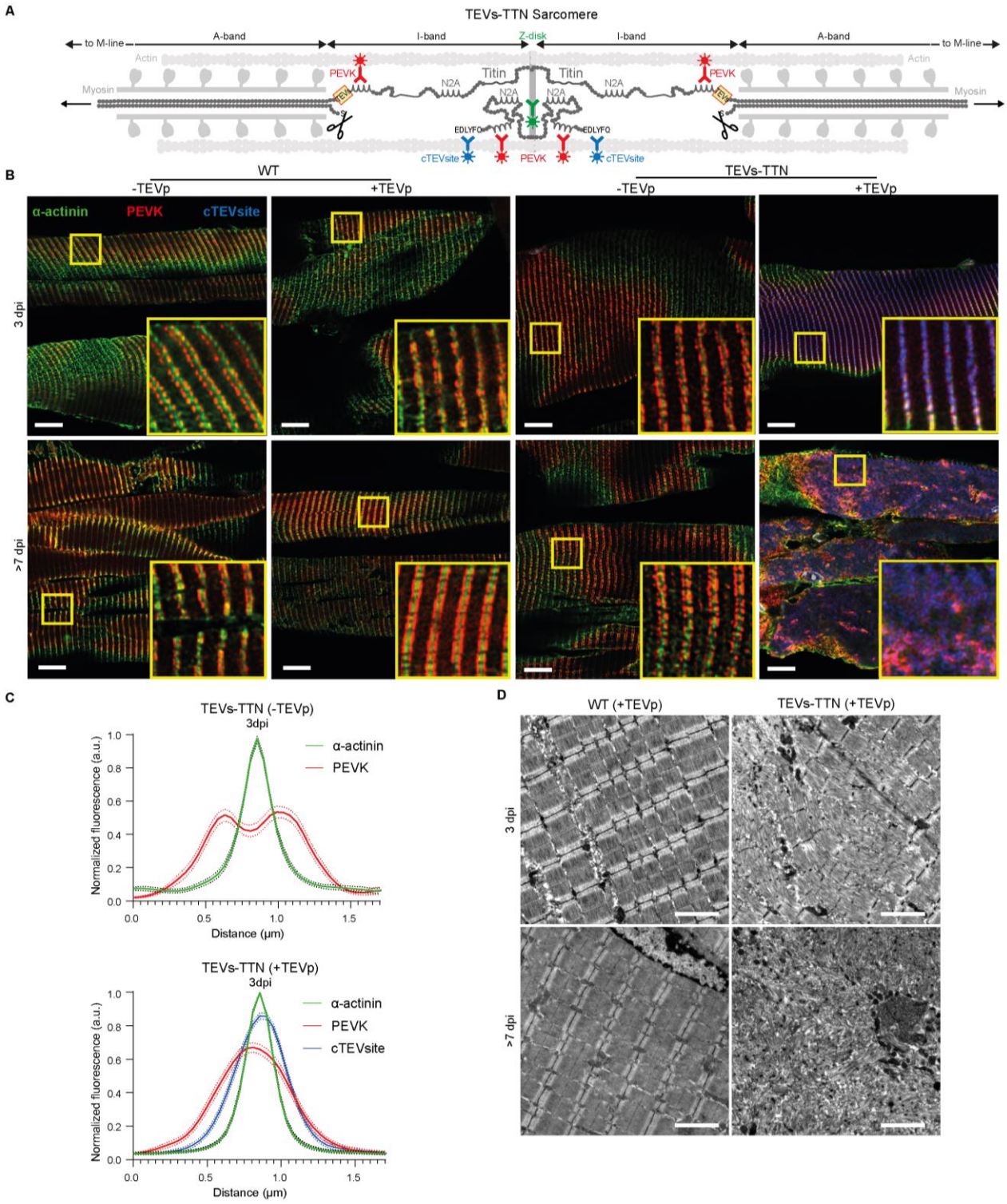

Figure 4. Progressive sarcomeric disassembly in titin mKO muscles. (A) Scheme of two half sarcomeres in TEVs-TTN muscles. TEV sites are represented by yellow boxes. The C-terminal sequence resulting from TEV cleavage is indicated. This epitope is recognized by anti-cTEVsite antibody only in cleaved titin. The scheme shows recoiling of cleaved titin. **(B)** Triple α-actinin/PEVK-titin/cTEVsite immunofluorescence on EDL longitudinal sections at different time points. Scale bars represent 10 µm. **(C)** Relative distribution of α-actinin, PEVK-titin and cTEVsite fluorescent signals in vehicle and AAV6-injected conditions at 3 dpi (76-102 sarcomeres analyzed from 17-24 myofibers extracted from 3-5 muscles per group). For AAV6-injected TEVs-TTN muscles, only cTEVsite-positive myofibers were assessed. **(D)** Transmission electron microscopy longitudinal sections of EDL myofibers at different time points (representative images of n=2-4 samples). Scale bars represent 2 µm. Data are represented as mean ± SEM.

807

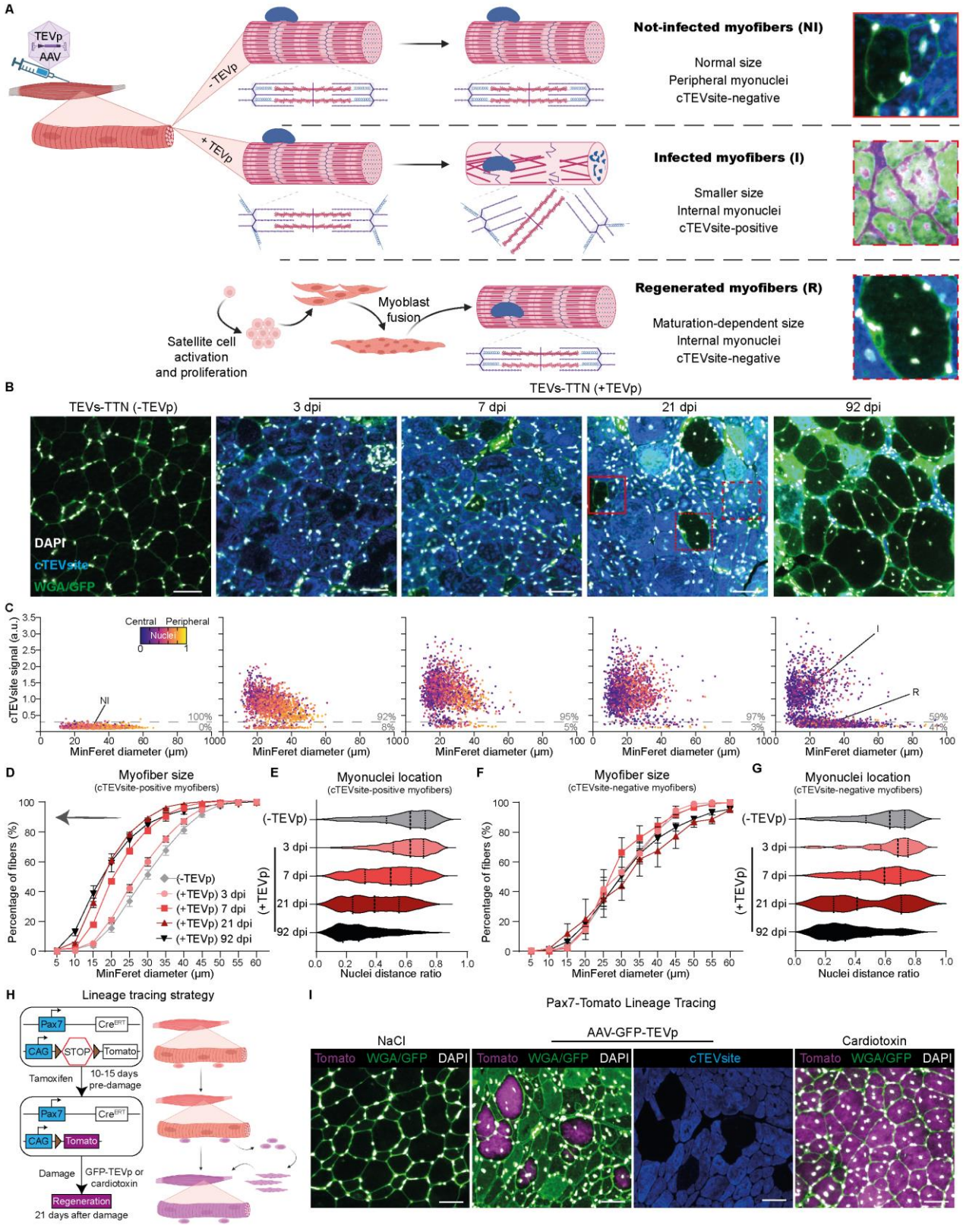

Figure 5. Coexistence of regenerative and titin mKO myofibers. (A) Scheme of the different types of TEVs-TTN myofibers expected after AAV6-GFP-TEVp infection. Non-infected myofibers have normal size, peripheral myonuclei and are negative for cTEVsite staining. Infected myofibers are small, show internal myonuclei and are stained by anti-cTEVsite antibody. Regenerative myofibers originating from satellite cell proliferation and fusion have variable size, internal myonuclei and are expected to be less cTEVsite-positive as a result of dilution of GFP-TEVp-expressing, non-replicative AAV6 viral particles during satellite cell proliferation. **(B)** DAPI/WGA-GFP/cTEVsite triple

immunofluorescence allows visualization of myofiber size, myonuclei position and cTEVsite signal for every myofiber. Scale bars represent 50 µm. **(C)** Quantification of cTEVsite signal, myofiber diameter and myonuclei-to-myofiber-centroid distance for every myofiber at the different time points (n= 2056 randomly chosen myofibers from 4-5 muscles per group, cTEVsite-positive threshold marked as dashed grey line). **(D, E)** Distribution of the MinFeret myofiber diameter (D) and violin plot of myonuclei distance ratio (E) in cTEVsite-positive myofibers (n= 1710-3663 myofibers from 4-5 muscles per group). **(F,G)** Distribution of the myofiber MinFeret diameter (F) and violin plot of myonuclei distance ratio (G) in cTEVsite-negative myofibers (n= 69-2059 myofibers from 4-5 muscles per group). **(H)** Scheme of lineage tracing experiment based on the elimination of STOP codons upon tamoxifen-induced Cre recombination in Pax7-expressing cells. In this strategy, regenerative myofibers originating from satellite cells are fluorescently labelled by a Tomato reporter. **(I)** Immunofluorescence identifies Tomato-positive regenerative myofibers in AAV6-GFP-TEVp-injected TEVs-TTN muscles surrounded by many Tomato-negative, cTEVsite-positive counterparts. A positive control of regeneration using cardiotoxin is also shown. Representative images from n=4-5 animals. Scale bars represent 50 µm.

808

809

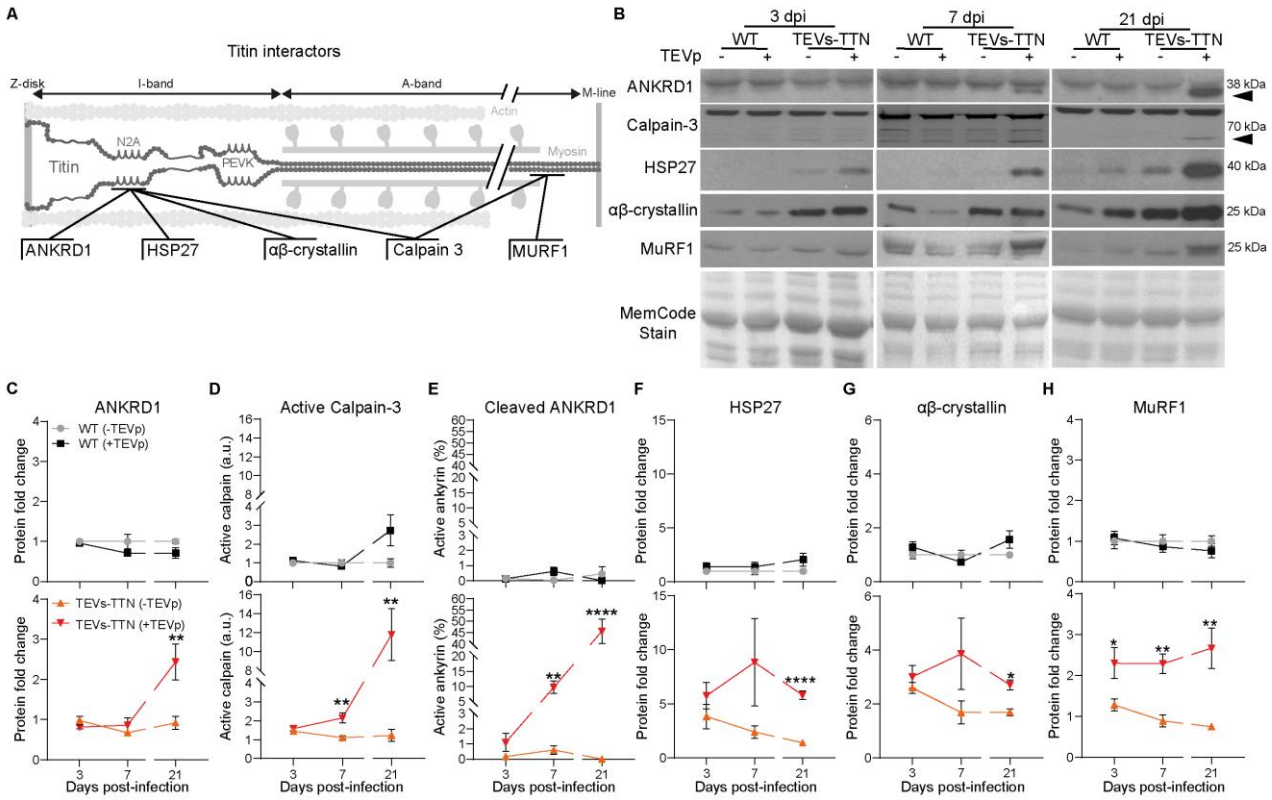

Figure 6. Levels of titin interactors in titin mKO muscles. (A) Scheme representing the binding sites of several titin interactors. **(B)** Protein expression of the different titin interactors evaluated by WB. The arrowheads mark active calpain-3 and cleaved ANKRD1. MemCode membrane staining was used for normalization. **(C-H)** Quantification of WB results (n=3-6). Cleaved ANKRD1 was calculated as the fraction of cleaved ANKRD1 relative to total ANKRD1. Cleaved calpain-3 was similarly calculated and the result was normalized to WT NaCl-injected samples. Protein fold changes were calculated relative to WT NaCl-injected samples. Data are represented as mean ± SEM.

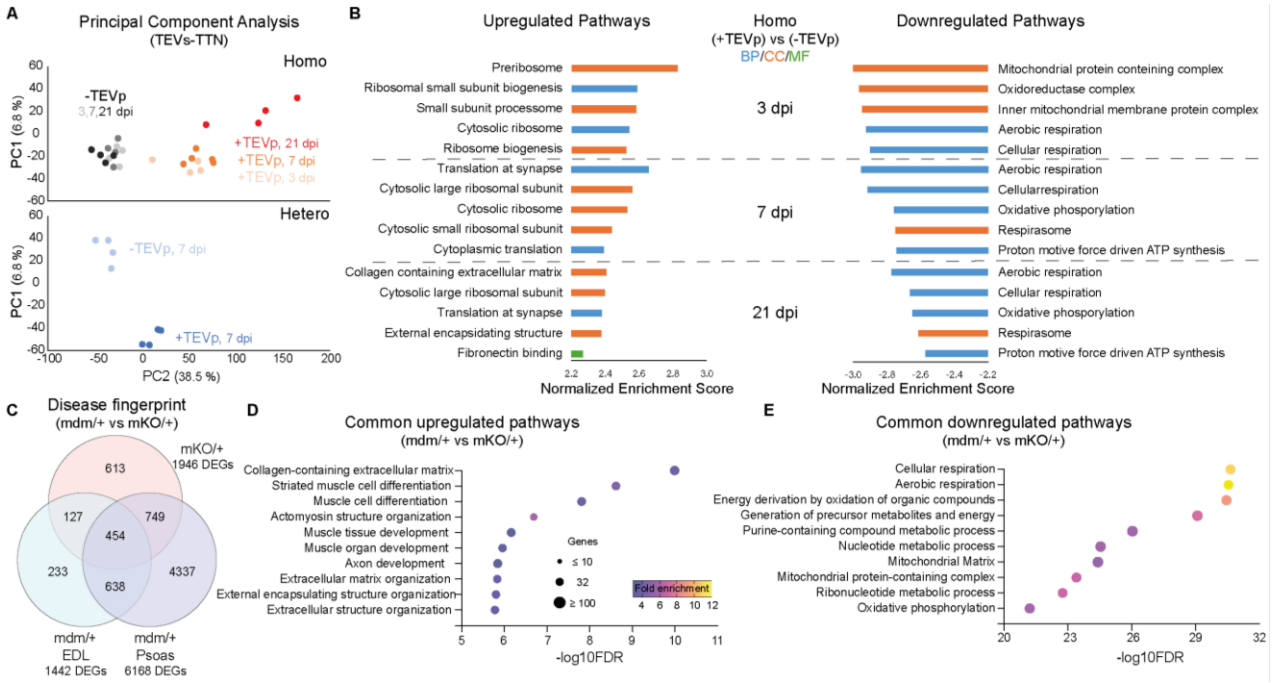

Figure 7. Myopathic transcriptional state of titin mKO muscles. (A) Principal component analysis of gene expression in homozygous and heterozygous TEVs-TTN TA muscles (n=4). **(B)** Top 5 most enriched upregulated and downregulated gene ontology terms in AAV6-injected homozygous TEVs-TTN muscles relative to contralateral control legs (BP: Biological process, CC: Cellular component, MF: Molecular function). **(C)** Shared differentially expressed genes in heterozygous titin mKO muscles, and heterozygous *mdm* EDL and psoas muscles[59]. **(D,E)** Top 10 most upregulated and downregulated gene ontology terms of the 1330 shared DEGs between heterozygous titin mKO at 7 dpi and heterozygous EDL and psoas *mdm* muscles.

811